



1 **Turbulent dissipation from AMAZOMIX off the Amazon shelf along** 2 **internal tides paths**

3 Fabius Kouogang^{1,4}, Ariane Koch-Larrouy¹, Jorge Magalhaes², Alex Costa da Silva⁴, Daphne Kerhervé¹,
4 Arnaud Bertrand⁵, Evan Cervelli³, Jean-François Ternon⁵, Pierre Rousselot⁶, James Lee⁷, Marcelo
5 Rollnic⁷, Moacyr Araujo⁴

6 ¹LEGOS, Université de Toulouse, CNRS, OMP, IRD, Toulouse, France

7 ²Department of Geoscience, Environment and Spatial Planning (DGAOT), Faculty of Sciences, University of Porto, Porto,
8 Portugal

9 ³Rockland Scientific Inc, Lunenburg, Nova Escócia, Canadá

10 ⁴Departamento de Oceanografia, Universidade Federal de Pernambuco, DOCEAN/UFPE, Recife, Brazil

11 ⁵MARBEC, Université de Montpellier, CNRS, Ifremer, IRD, Sète, France

12 ⁶IMAGO, Université de Bretagne Occidentale, CNRS, Ifremer, IRD, Brest, France

13 ⁷Departamento de Oceanografia, Universidade Federal do Para, UFPA, Belem, Brazil

14 *Correspondence to:* Fabius Kouogang (fabius.cedric@yahoo.fr)

15 **Abstract.**

16 The Amazon shelf-break is a key region of the ocean where strong internal tides (ITs) are generated, which may have a key
17 role to play on both Climate and Ecosystem, via its vertical mixing. AMAZOMIX survey (2021) collected microstructure and
18 hydrographic (ADCP/CTD-O₂) profiles to quantify mixing, associated processes and their impact on marine ecosystems.
19 Measurements are obtained over M2 tidal period (12h) inside and outside of both the ITs generation sites and propagation
20 beams, respectively at mode-1 distances (90km and 210km) from the shelf-break to evaluate the IT impact on mixing.

21 Hydrography analysis showed strong step-like characteristics (~20-40 m thick) and vertical displacements (20-60 m) triggered
22 by ITs, as well as the signatures of high modes up to 5-6 on generation sites and IT pathways.

23 The results of the microstructure analysis coupled with those of the hydrography revealed important mixing associated with a
24 competition of processes between the semidiurnal shear of ITs and the baroclinic shear of the mean current (BC). Closer to the
25 generation sites, mixing is stronger within $[10^{-6}, 10^{-4}]$ W.kg⁻¹, with a greater contribution (~65 %) from ITs shear than BC shear.
26 It is reduced but nevertheless considerable between $[10^{-8}, 10^{-6}]$ W.kg⁻¹ along the IT pathways, owing to equal contributions
27 from ITs and BC shear. At a distance of ~225 km, mixing was still higher within $[10^{-7}, 10^{-6}]$ W.kg⁻¹ because of the increased
28 contribution (~65 %) of ITs shear, where IT beams may intersect and interact with background circulation. Mixing in no-tidal
29 fields was fairly minimal ($[10^{-8}, 10^{-7}]$ W.kg⁻¹), owing to a minor contribution (~50.4 %) of BC shear from the North Brazil
30 Current.



31 Finally, the nutrient flux estimations showed that ITs mixing could reach the surface (by a large tidal diffusivity of $[10^{-4}, 10^{-1}]$
32 $\text{m}^2 \cdot \text{s}^{-1}$). This resulted in high vertical fluxes of nitrate ($[10^{-2}, 10^{-0}] \text{mmol N m}^{-2} \cdot \text{s}^{-1}$) and phosphate ($[10^{-3}, 10^{-1}] \text{mmol P m}^{-2} \cdot \text{s}^{-1}$),
33 which can stimulate chlorophyll production, biodiversity and cool surface water, so influencing the whole ecosystem and
34 climate in this river-ocean continuum region. This study provides a guide for the mixing parameterization in future numerical
35 simulation (e.g., in physical-biogeochemical coupled models) in the Amazon region in order to include the impact of the IT
36 turbulence on the whole ecosystem (i.e., from physics to biological production).

37 **1 Introduction**

38 Turbulent mixing in the ocean plays an important role for sustaining the thermohaline and meridional overturning circulation
39 (Kunze, 2017) and for closing the global ocean energy budget. These processes have strong implications for the climate,
40 through the influence on heat and carbon transport, and nutrient supply for photosynthesis (Huthnance, 1995; Munk and
41 Wunsch, 1998). Mixing processes can result from wind in the surface layer of the ocean, internal waves and shear instability
42 in the ocean interior, and bottom friction close to the bottom layer (Miles, 1961; Thorpe, 2018; Ivey et al., 2020; Inall et al.,
43 2021). Barotropic tides interacting with steep shelf-break topography trigger internal waves at tidal frequency and harmonics
44 called internal tides (ITs) that may propagate and generate mixing. These ITs induce large vertical displacements of water
45 masses up to tens of metres. After their generation at shelf-break, ITs higher-modes (more unstable) can dissipate locally
46 whereas ITs lower-modes may propagate far from generation sites. They can dissipate where the energy beam reflects at the
47 bottom, at the surface or at the thermocline levels (Bordois, 2015; Zhao et al. 2016) or where energy flux interferes with each
48 other (Zhao et al. 2012). ITs can also dissipate when they interact with strong baroclinic eddies or currents (Rainville and
49 Pinkel, 2006; Whalen et al., 2012). Furthermore, ITs may disintegrate in packets of higher-mode nonlinear internal solitary
50 waves (ISWs) that can propagate and dissipate offshore (Jackson et al., 2012).

51 Previous and recent studies have reported that ITs-induced turbulent mixing can have impacts on the surface, such as on sea
52 surface temperature (Ray and Susanto, 2016; Nugroho et al. 2018; Assene et al., 2024), chlorophyll content (M'Hamdi et al.,
53 2024; in preparation) and marine ecosystems (Wang et al. 2007; Muacho et al., 2014; Zaron et al. 2023), as well as on the
54 atmospheric convection and the rainfall structure (Koch-Larrouy et al., 2010, Sprintall et al. 2014).

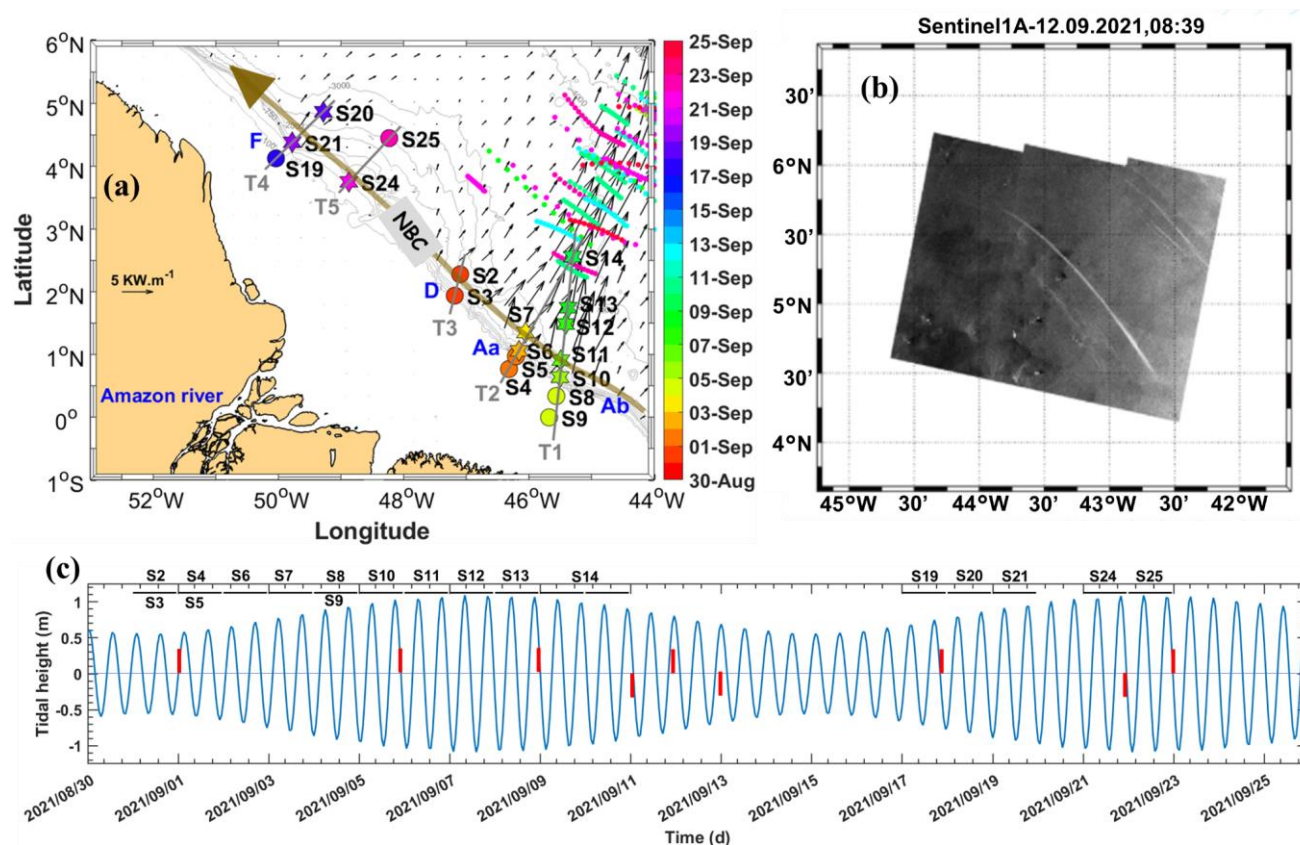
55 In the western tropical Atlantic, the Amazon River-Ocean Continuum (AROC) constitutes a key region of the global oceanic
56 and climate system (Araujo et al., 2017; Varona et al., 2018). This region is characterised by the presence of a system of
57 western boundary currents including North Brazil Current (NBC). NBC flowing northwestward has its core velocities (~ 1.2
58 $\text{m} \cdot \text{s}^{-1}$) stable from the surface to a depth of 100 m (Johns et al., 1998; Bourlès et al., 1999; Barnier et al., 2001; Neto and Silva,
59 2014). There is also a system of Amazonian Lenses of water (AWL) induced by continental inputs, which can influence both
60 boundary layer and mixed layer patterns (Silva et al., 2005; Prestes et al., 2018).

61 In the AROC region, the Amazon shelf-break is a hotspot for generation, propagation and dissipation of ITs and ISWs as a
62 result of non-linear processes (Geyer, 1995; Magalhães et al., 2016; Ruault et al., 2020; Tchilibou et al., 2022; Figure 1). Using



63 SAR images, previous studies (Magalhaes et al., 2016) identified ISWs along the path of ITs propagating from two sites (i.e.,
64 sites Aa and Ab; Fig. 1a). Conversely, other sites did not have any ISW propagation (i.e., sites F and D; Fig. 1a and 1b) (see
65 Magalhaes et al., 2016 for definition). Using numerical modeling, Tchilibou et al. (2022) showed that about 30% of the M2
66 (dominant tidal component, Le Bars et al. 2010) ITs energy is dissipated locally (for higher-modes ITs) at sites F, Aa, Ab and
67 D (Fig. 1a), and that the remaining lower-modes ITs energy can be dissipated remotely. Dissipation away from the generation
68 sites (F, Aa, Ab and D; Fig. 1a) can result from the shear instabilities that are due to processes of ITs-ITs and/or ITs-
69 eddy/current interactions. Despite the presence of ITs, no direct measurements of dissipation rates have been conducted. In
70 addition, the impacts of IT dissipation on vertical nutrient fluxes in the AROC region are still unexplored.

71 The mixing induced by these internal waves in the region was observed during the AMAZOMIX cruise (Bertrand et al., 2021).
72 It has been designed to have stations/transects inside and outside ITs fields (Fig. 1a) and to measure ITs dissipation and study
73 their impact on the AROC ecosystem. Direct microstructure measurements of temperature, salinity and velocity were
74 conducted at the different repeated stations/transects over one M2 tidal cycle (~12h). In this study, we will quantify mixing,
75 identify the associated processes, and investigate their impact on nutrient fluxes off the Amazon shelf. We will calculate
76 turbulent kinetic energy (TKE) dissipation rates and vertical eddy diffusivities using in situ microstructure and hydrography
77 data. The baroclinic shear of currents will then be calculated from current data collected between stations and transects. Finally,
78 we will use vertical diffusivities estimations to determine vertical nutrient fluxes at the base of the mixed layer.



79
 80 *Figure 1: a) Map of part of the AMAZOMIX 2021 cruise with bathymetric grey lines (100 m, 750 m, 2000 m, 3000 m and 4000*
 81 *m isobaths) off the Amazon shelf. Colored circles and stars represent short and long CTD-O₂/L-S-ADCP stations casts,*
 82 *respectively. Colored bar represents the time. Solid grey lines represent SADCPC transects (T1 to T5). Black arrows represent*
 83 *25h-mean depth-integrated baroclinic energy flux (on September 2015 from NEMO model) from ITs generation sites (Aa, Ab,*
 84 *D and F) along the critical slope (grey contours) of the shelf-break. Solid brown line indicates the background circulation*
 85 *with NBC pathways. Shattered colored lines show ISW signatures. T1 to T4 and T5 represent the inside-ITs and outside-ITs*
 86 *transects, respectively. b) 1A Sentinel image acquired 12th September 2021 showing ISW signatures. c) Tidal range at*
 87 *AMAZOMIX stations with ISW signatures dates in red bars.*

88

89 2 Data and Methods

90 2.1 Data collection

91 The AMAZOMIX cruise (Bertrand et al., 2021) was performed on the shelf/slope areas off the AROC during August-October
 92 2021, on board the IRD vessel RV ANTEA. 12h-long stations were conducted with repeated (between 4 and 5 for each site)
 93 casts of Conductivity-Temperature-Depth-Oxygen (CTD-O₂)/Lowered Acoustic Doppler Current Profiler (LADCP) and



94 Velocity Microstructure Profiler (VMP) in previously defined sites to measure the TKE dissipation rates over one complete
95 tidal cycle, and extract the tidal (M2) contribution from the total current. A high-resolution NEMOv3.6 model (1/36°) (Nucleus
96 for European Modeling of the Ocean; Madec et al., 2019) that provides realistic maps of ITs generation and propagation (Fig.
97 1a; Tchilibou et al., 2022; Assene et al., 2024) was used to estimate the position of 12h stations and estimate the mean
98 background stratification at these stations. Stations (Fig. 1a and 1c) were located inside the ITs fields, named “IN-ITs” (sites
99 Aa, Ab and D: S2 to S14; site F: S19 to S21), and outside the ITs fields (S24 and S25), named “OUT-ITs”, on the shelf-break
100 generation (sites Aa, Ab, D and F) and propagation along 5 transects (T1 to T5, Fig. 1) including stations.

101 CTD-O₂ measurements were obtained using a Seabird 911 Plus with dual sensors mounted in the rosette equipped with 11
102 Niskin bottles used to sample water down to a depth of 1000 m. Concentrations of nutrients, including nitrate and phosphate,
103 were determined from nutrient samples taken in 30 ml Nalgene bottles and stabilised in an oven at 80 °C for 2h30. The 24 Hz
104 CTD-O₂ sensors were calibrated before and after the cruise. The standard deviation of temperature (salinity; oxygen) was
105 0.003 °C (0.003 PSU; 0.05 ml.l⁻¹) according to adjusted data. CTD-O₂ data were averaged over 1-m bins to filter out spikes
106 and missing points, and aligned in time to correct the lag effects. Two LADCPs RDI 300 kHz were mounted on the rosette,
107 one looking down and other one looking up, to provide vertical currents profiles with a 8 m resolution. In addition, 75 kHz
108 ship-ADCP (SADCP) profiles (with vertical resolution adjusted to the bottom depth: 8 m at S6, S7, S10-S14, S20, S21 and
109 S24, for bottom depth > 150 m; and 4 m at the rest) were continuously recorded during the cruise. All measured data were
110 processed and quality controlled according to the standard protocols of the GO-SHIP Repeat Hydrography Manual. A total
111 number of 71 CTD-O₂/LADCP profiles were acquired during the AMAZOMIX cruise.

112 To characterize mixing, the TKE microstructure profiles were obtained from high frequency (resolution: ~2 mm)
113 measurements of temperature and velocity shear using a VMP-250 profiler (Rockland Scientific International, Inc.) operating
114 at depth range of 1000 m. The instrument has two high-resolution thermistors (FP07) and two high-resolution velocity shear
115 probes (probe 1 and 2, with accuracy of 5 % of the total signal) with their sampling frequency of 1024 Hz. The VMP-250
116 profiler was deployed and recovered with use of an electric winch and rope tether. The VMP was alternatively deployed
117 between the CTD-O₂/LADCP profiles at 33 stations for a total of 202 profiles. Only 18 stations (S2 to S14, S19 to S21, S24
118 and S25) for a total of 109 VMP profiles and 54 CTD-O₂/LADCP profiles will be processed and used in this study.

119 **2.2 Methods**

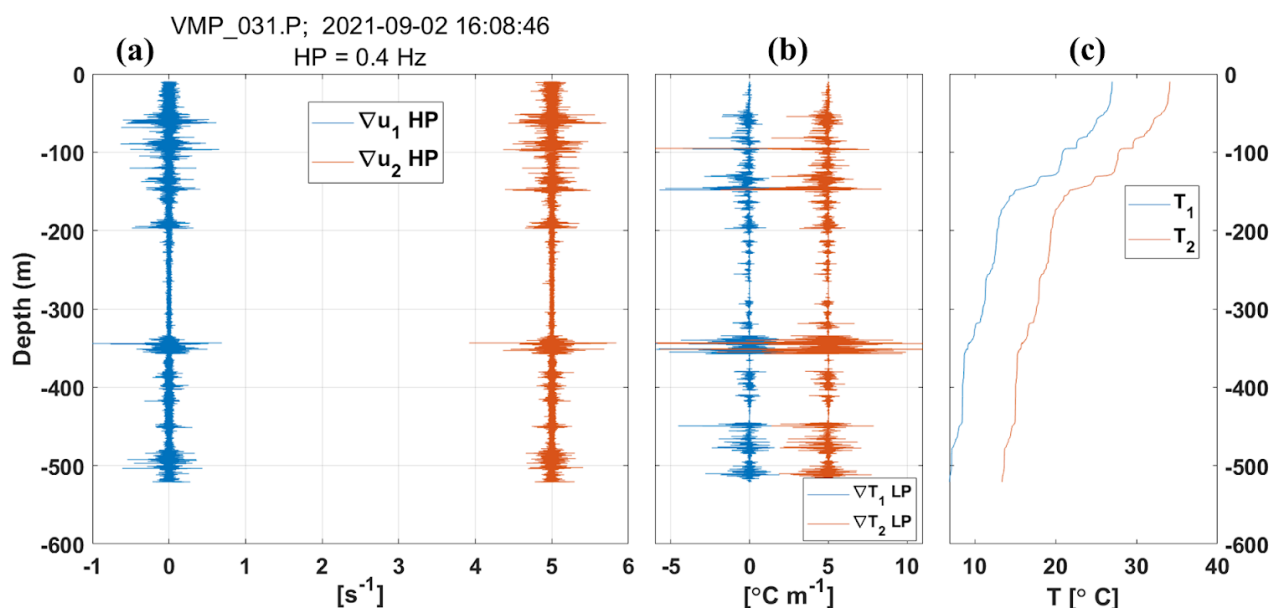
120 **TKE dissipation rates**

121 VMP data were processed using ODAS Matlab library (developed by Rockland Scientific International, Inc) in order to
122 determine TKE dissipation rate (ϵ). The VMP processing methods are briefly explained here, and conform to the
123 recommendations of ATOMIX (Analyzing ocean turbulence observations to quantify mixing) group (reported in Lueck et al.,
124 2024) and tested against the benchmark estimates (presented in Fer et al., 2024). First, the VMP data are converted into physical
125 shear units. The time series are prepared, and sections (continuous parts of the time series) within VMP data are chosen for
126 dissipation estimation. Before spectral estimation, the aberrant shear caused by vessel wake contamination is eliminated from



127 the timeseries. Shear probe collisions (with plankton and other matter) are removed from the shear signals using the de-spiking
 128 routine. The record from each section is high-pass filtered. Shear spectra are estimated using record lengths (`diss_length`) and
 129 Fast Fourier Transform segments (`fft_length`) of 2s that are cosine windowed and overlapped (`overlap_sec`) by 50%. Vibration-
 130 coherent noise is removed. Different `diss_length` and `overlap_sec` were chosen and tested based on the environment (deep and
 131 shallow water) following Fer et al. (2024). After testing, the `diss_length` (`overlap_sec`) was shortened to 4s (2s) for shallow
 132 stations rather than 8s (4s) for deep stations, because of the evidence of the presence of overturns from AMAZOMIX acoustic
 133 measurements in deep water stations (Koch-Larrouy et al., 2024; in preparation) and to optimize the spatial resolution of
 134 dissipation estimates in shallow water stations. Finally, ϵ is determined using the spectral integration method and by
 135 comparison with the Nasmyth empirical spectrum (Nasmyth, 1970).

136 The estimation of ϵ used high pass filtered data. Fig. 2 shows an example of the high pass filtered shear probes data at station
 137 S6 (Fig. 2a). The shear data are qualitatively supported by both the observed profiles (Fig. 2c) and the low-pass filtered, along-
 138 path gradients (Fig. 2b). Hence, in high turbulence regions, the temperature gradient variance is enhanced (bipolar), and the
 139 temperature is reversed as a result of the overturns. In low turbulence regions, the temperature gradient variance is inverted
 140 and background temperature tends to decrease with depth.



141
 142 *Figure 2: Example of the VMP data at station S6. (a) Vertical profiles of data from shear probe 1 (∇u_1 , blue), and from shear*
 143 *probe 2 (∇u_2 , red). HP indicates high-pass filtering of the shear probe data. (b) Vertical gradients of temperature from shear*
 144 *probe 1 (∇T_1 , blue) and probe 2 (∇T_2 , red). LP indicates low-pass filtering on the along-path gradients. (c) Temperature*
 145 *profiles T_1 (blue) and T_2 (red) based on nominal calibration coefficients.*

146



147 For each of the CTD-O₂ profiles, the Mixed Layer Depth (MLD) was computed using a density criterion of 0.03 kg.m⁻³
148 difference (Montégut et al., 2004) with the surface density (with no major difference from density criterion of 0.01 and 0.02
149 kg.m⁻³ by way of comparison) at AMAZOMIX stations/transects. Based in Lozovatsky et al (2006) and Sutherland et al (2014),
150 the miXed Layer Depth (XLD) is determined where ϵ falls to an assumed background level (first minimum value) in order to
151 capture the dissipation rate away from the influence of sea surface processes. The Upper (UTD) and Lower (LTD/LPD)
152 Thermocline/Pycnocline Depth was delimited as defined by Assunção et al (2020). UTD corresponded to the depth where the
153 vertical temperature gradient $\partial\theta/\partial z = 0.1$ °C.m⁻¹, while LTD/LPD were the last depth below the UTD at which $N^2 \geq 10^{-4}$ s⁻².

154

155 **Vertical eddy diffusivity and turbulent flux of nutrients**

156 The vertical eddy diffusivity coefficient (K_z) is calculated from ϵ following Osborn (1980) formulation as defined by $K_z = \epsilon \Gamma$
157 N^{-2} . Here N^2 is the buoyancy frequency squared was calculated using the sorted potential density profiles (σ_θ) from CTD-O₂
158 profiles, via $N^2 = - (g/\rho_0) (d\sigma_\theta/dz)$ where ρ_0 is a reference density (1025 kg.m⁻³) and g is the gravitational acceleration. Γ is a
159 mixing efficiency defined as the ratio between the buoyancy flux and the energy dissipation, and is set to 0.2 which corresponds
160 to the critical Richardson number $Ri = 0.17$ based in Osborn (1980). ϵ was linearly interpolated into the depths of N^2 .

161 The vertical turbulent flux F (unit: mmol.m⁻².s⁻¹) of nutrients (nitrate and phosphate) was estimated from K_z as defined by:

$$162 F_{(NO_3^-, PO_4^{3-})} = -K_{(NO_3^-, PO_4^{3-})} \left(\frac{\partial C_{(NO_3^-, PO_4^{3-})}}{\partial z} \right), \quad (1)$$

163 where $C_{(NO_3^-)}$ and $C_{(PO_4^{3-})}$ indicates the concentration of nitrate (NO₃⁻) and phosphate (PO₄³⁻) (unit: mmol.L⁻¹), respectively,
164 and $K_{(NO_3^-)}$ and $K_{(PO_4^{3-})}$ indicates its vertical diffusivity, respectively. Here we assume $K_{(NO_3^-, PO_4^{3-})}$ is equivalent to K_z . The
165 vertical profiles of nutrient concentrations (obtained from bottle sampling) were linearly interpolated into the depths of K_z .

166

167 **Baroclinic currents and energy**

168 To evaluate the processes that can explain the mixing measured, the baroclinic (u' , v') components of horizontal velocity was
169 calculated ($u' = u - u_{bt}$, $v' = v - v_{bt}$) removing the barotropic (u_{bt} , v_{bt}) components of total horizontal current (u , v)
170 provided by SADCP time series with LADCP profiles glued below ~ 500 m of depth, as shown by the equations below.

$$171 [u', v'] = [u, v] - [u_{bt}, v_{bt}], \quad (2)$$

$$172 [u_{bt}, v_{bt}] = \frac{1}{H} \int_{-H}^0 [u, v] dz \quad (3)$$

173 The M2 tidal component of baroclinic currents is evidenced by baroclinic (semi-diurnal) tidal velocity (u'' , v'') by removing
174 ($[u'', v''] = [u', v'] - [\bar{u}', \bar{v}']$, with overbar the average over a tidal period) the baroclinic mean current (\bar{u}' , \bar{v}') profile, and
175 highlighted by baroclinic (semi-diurnal) tidal shear squared $S^{2''}$ ($S^{2''} = (\partial u''/\partial z)^2 + (\partial v''/\partial z)^2$) compared at the baroclinic mean
176 vertical shear squared $\overline{S^{2'}}$ ($\overline{S^{2'}} = (\partial \bar{u}'/\partial z)^2 + (\partial \bar{v}'/\partial z)^2$). The vertically sheared total baroclinic current can be converted to total
177 baroclinic energy following internal waves parameterization of dissipation rates (ϵ_{MG}) by Mackinnon and Gregg (2003) and
178 validated by Xie et al. (2013), as defined by:



179 $\varepsilon_{MG} = \varepsilon_0 (N/N_0) (S/S_0),$ (4)

180 with N the buoyancy frequency from CTD-O₂ profiles and S the vertical shear from baroclinic currents. $N_0=S_0=0.0052 \text{ s}^{-1}$ and
181 $\varepsilon_0=2.2 \cdot 10^{-9} \text{ W.kg}^{-1}$ (adjustable constant). By simple substitution in this formulation, we computed the baroclinic tidal energy
182 (ε''_{MG}) and baroclinic energy of mean circulation ($\overline{\varepsilon'}_{MG}$) in order to obtain the individual contribution ($\overline{\varepsilon'}_{MG}/(\overline{\varepsilon'}_{MG} + \varepsilon''_{MG})$ for
183 mean baroclinic energy and $\varepsilon''_{MG}/(\overline{\varepsilon'}_{MG} + \varepsilon''_{MG})$ for M2 semi-diurnal baroclinic energy) to the total baroclinic energy ($\overline{\varepsilon'}_{MG} +$
184 ε''_{MG}).

185 To evaluate the bottom friction effect, the kinetic energy $\varepsilon_f = \frac{1}{2} \rho_s (u_f^2)$ close to the bottom boundary layer was computed using
186 friction velocity $u_f = u_b \sqrt{C_d}$. $C_d=2.5 \cdot 10^{-3}$ is the drag coefficient from a high-resolution NEMOv3.6 model (1/36°) (Nucleus
187 for European Modeling of the Ocean; Madec et al., 2019). Previous study of Huang et al. (2019) shown that the bottom
188 boundary thickness spatially varies between 15-123 m in Ocean Atlantic with median of about 30-40 m in the North Atlantic.
189 Bottom layer thicknesses were defined in our study area depending on the measured bathymetry from CTD-O₂ and near-bottom
190 currents from ADCP. u_b is the total velocity over 15 m (40 m) thick above the seabed for shallow (deep) stations.

191
192 **Ray tracing calculation**

193 Analysing both the vertical profiles of the average currents and the spatial dimension along the IT pathways is another way to
194 better understand the mechanisms related to the measured mixing. The rays of ITs energy are generated at steep topography
195 regions (e.g., shelf-break) where ITs beams and the bottom slope match together (i.e. critical slopes) and then propagate within
196 the ocean interior. After seafloor reflection, these IT beams propagate upward and impinge on the seasonal pycnocline from
197 below (resulting in beam scattering) and create large ITs oscillations, which after steepening have been documented to
198 disintegrate into nonlinear ISWs - known as a “local generation” for the ISWs (New and Pingree, 1992). Theoretical analysis
199 of IT paths was computed using IT ray-tracing techniques previously used (New and Da Silva, 2002; Muacho et al., 2014), to
200 investigate the effectiveness and expected pathways of the IT beams off the Amazon shelf. One main hypothesis we made
201 using linear theory is to consider that the stratification is constant horizontally along the IT propagation path. Whereas in
202 reality it may vary, due to submesoscale and mesoscale variability. The IT ray tracing calculation assumes that in a
203 continuously stratified fluid, ITs energy can be described by characteristic pathways of beams (or rays) with a slope c to the
204 horizontal following:

205 $c = \pm \left(\frac{\sigma^2 - f^2}{N^2 - \sigma^2} \right)^{1/2},$ (5)

206 where σ is the M2 tidal frequency ($1.4052 \times 10^{-4} \text{ rad.s}^{-1}$), and f is the Coriolis parameter. The N^2 from CTD-O₂ AMAZOMIX
207 data were first time-averaged to obtain the mean stratification at stations. Then, the monthly Amazon36 (2012-2016) N^2
208 obtained from NEMO model outputs (see Tchilibou et al., 2022; Assene et al., 2024, for model description) were smoothed
209 and stitched to the AMAZOMIX N^2 profiles below 1000m depth. IT ray-tracing diagrams were obtained along the 5 transects
210 (T1 to T5, Fig. 1a). Sensibility tests of IT rays with different seasons (August, September, October and April) were performed



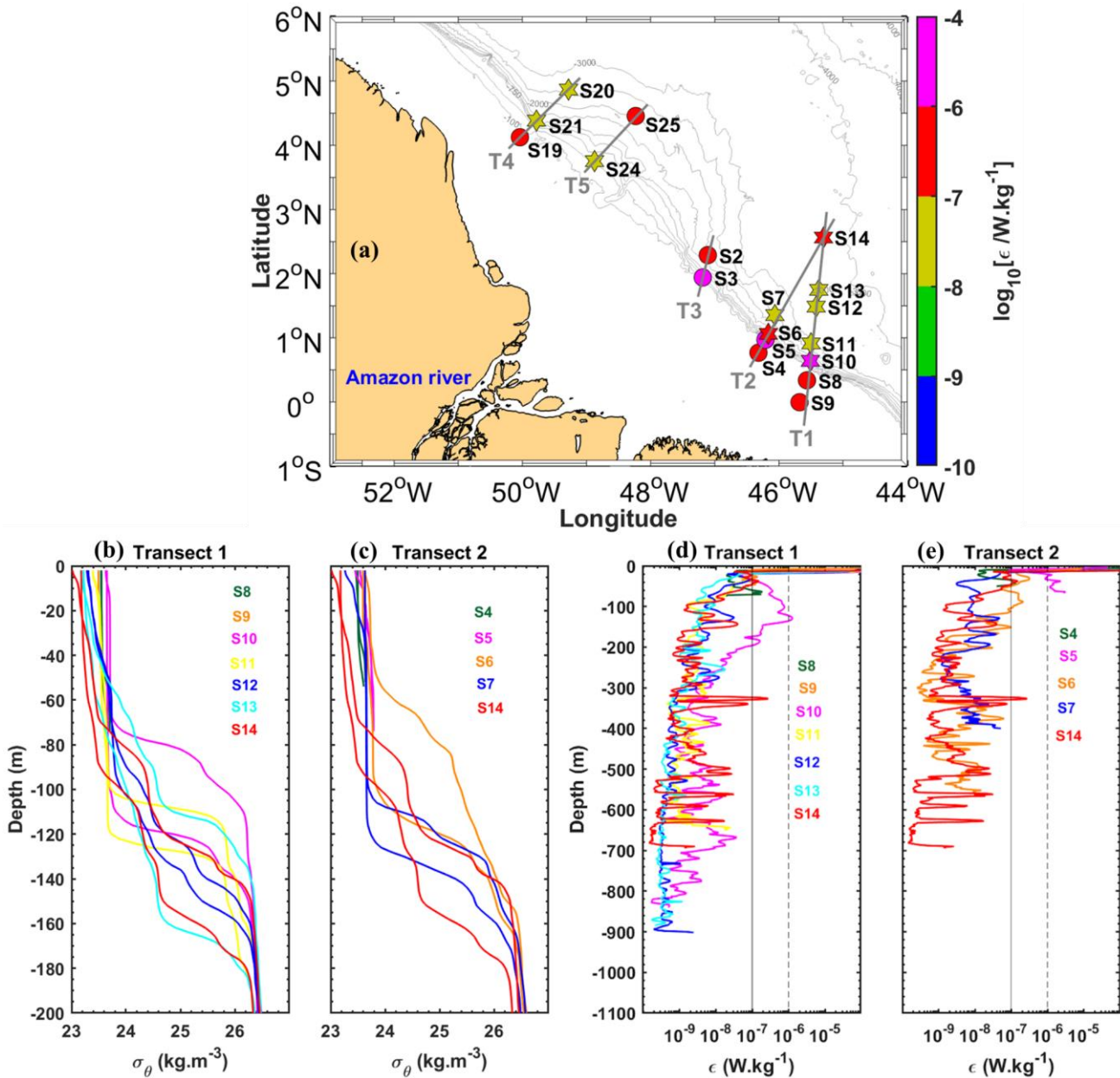
211 varying the position of critical topography in order to get an envelope of ray paths consistent with characteristics of IT
212 pathways.

213 **3 Results**

214 **3.1 Mixing**

215 **3.1.1 Thermohaline and IT features**

216 In this section we analyze density profiles to gain information on the mixing and/or on waves propagation. First we observe
217 step-like features in the density profiles (Fig. 3b and 3c). During the M2 tidal period, step-like structures of ~20-40 m thick
218 are found at depths ranging from 80-160 m at S10, S12, S13, and S14 (Fig. 3b). They are thicker along the IN-ITs transect T1
219 than along other transects (T2–T4) (Fig. A1.a and A1.b, Appendix). Then, between 60 and 170 m depth, large vertical
220 displacements of 20 to 60 m are detected along T1-T2 and T4 (e.g., 40 m at S10, 48 m at S6, 52 m at S13, and 32 m at S14)
221 (Fig. 3b and 3c). The smallest displacements (e.g., ~8 m at S25) are observed along OUT-ITs transect T5 (Fig. A1.b,
222 Appendix). Finally, the vertical displacement of the IT wave may also be detected in the variability of the mixed layer depth
223 (MLD), which ranges from 18 to 84 m over a semi-diurnal cycle (see Fig. 6.e). As a preliminary conclusion, both step-like
224 structures and isopycnal displacements support the hypothesis of propagating ITs, that can have stronger energy along transects
225 T1 and T2, weaker on T3, T4, and almost absent on T5 (Fig. 1a).



226
 227 Figure 3: (a) Horizontal (maximum) dissipation rates (ϵ , $W \cdot kg^{-1}$, on log scale) from VMP during the AMAZOMIX 2021 cruise
 228 for all stations/transects T1 to T5. (b)-(c) Density profiles (in $kg \cdot m^{-3}$) from CTD- O_2 and (d)-(e) vertical dissipation rates (ϵ in
 229 $W \cdot kg^{-1}$, on log scale) from VMP during the AMAZOMIX 2021 cruise for the transects/stations inside of the IT fields (b)-(d) T1
 230 (S8-S14) and (c)-(e) T2 (S4-S7 and S14). For long stations (S6, S7 and S10-14), two density profiles are used to illustrate the
 231 step-like structures and isopycnal vertical displacements along the transects. Colour is used to distinguish each station in each
 232 transect. Dashed and solid back lines (on panels c and d) are for comparison. The density of S4 and S5 vary between 23.4-
 233 23.8 kg/m^3 .



234

235 **3.1.2 TKE Dissipation rates and mixing**

236 Now, we analyze the distribution of dissipation rates (ϵ) estimated below the mixing layer depth (hereinafter XLD), in order
237 to characterize the mixing produced off the Amazon shelf. Note that the XLD (Table A1, Appendix) is generally deeper than
238 the MLD.

239 Results show that from the continental shelf to the open sea ϵ vary within the range of $[10^{-10}, 10^{-4}]$ W.kg^{-1} . Mapping the
240 maximum value of ϵ over the water column (Fig. 3a, 3d and 3e) reveals that the strongest ϵ within $[10^{-6}, 10^{-4}]$ W.kg^{-1} are
241 observed on IN-ITs transects (T1-T3), and even larger ϵ are found on the shelf-break at generation site of ITs (S3, S6 and S10).
242 Smaller ϵ values (between $[10^{-8}, 10^{-7}]$ W.kg^{-1}) are found away from the shelf-break (e.g., at S7, S11, S24 and S20), except at
243 some deep-sea stations (e.g., at S14 and S25).

244 The vertical profile of ϵ (Fig. 3d and 3e, and Fig. A1.c and A1.d, Appendix), show stronger ϵ (10^{-7} - 10^{-6} W.kg^{-1}) in the
245 thermocline layers (~ 120 m) for the stations close to the shelf-break and in the ITs influence (S6 and S10). Hotspots of mixing
246 are found almost anywhere at S14 in the water column, for example, at 150, 300, 350, 500, 600 and 700 m depth. Finally for
247 shelf stations in the ITs regions, S3 and S5, mixing increases close to the bottom.

248 As another preliminary conclusion, the distribution of ϵ ranges by 2-3 orders of magnitude over depth, and indicates stronger
249 mixing on the Amazon shelf and shelf-break compared with those located far from these areas, and even stronger in the regions
250 of occurrences of ITs. In order to investigate the precise reasons for such heterogeneous distribution of ϵ the aim of the next
251 section will be to try to identify the different processes responsible for it, by looking at shear instability driven by the current
252 measurements.

253

254 **3.2 Processes contributing to mixing**

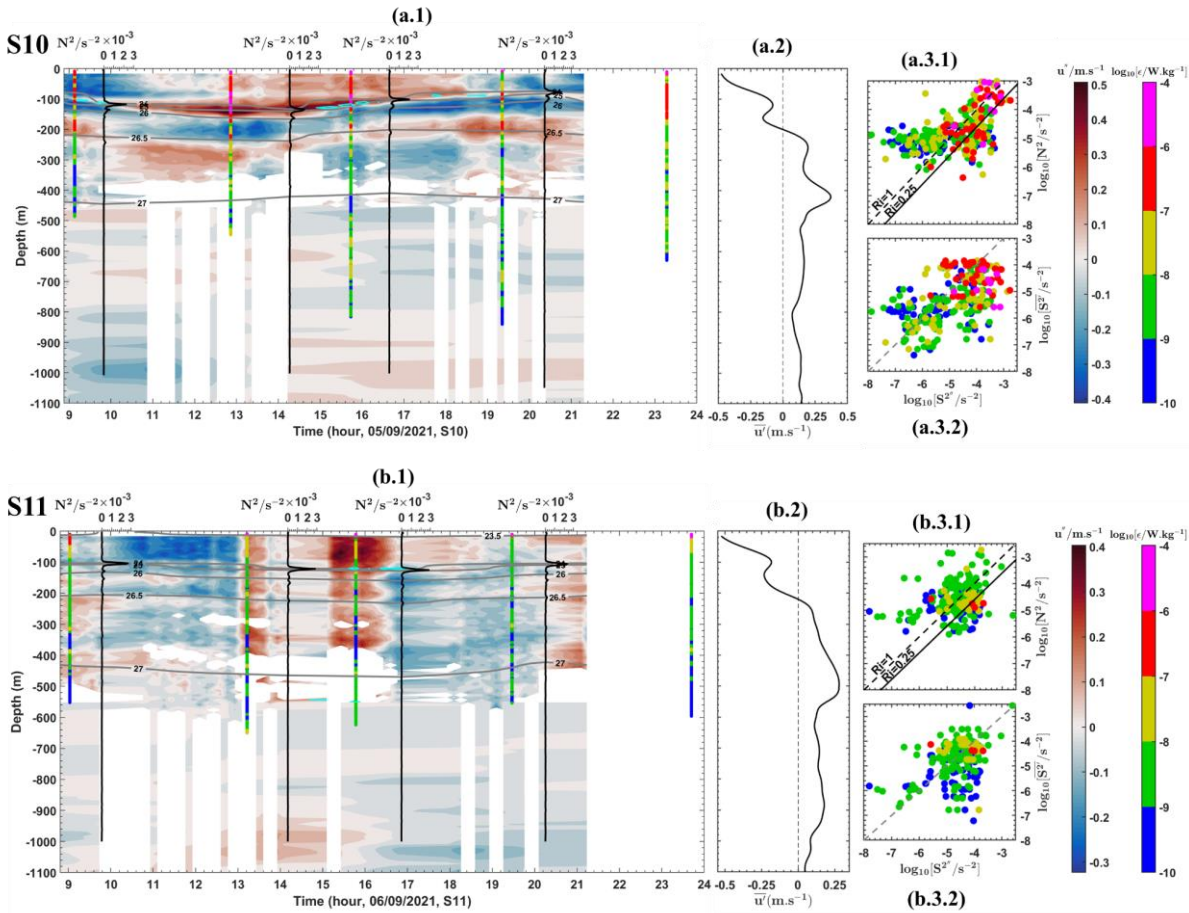
255 In this section, we explore which processes among tides, general circulation, and friction are responsible for the high mixing
256 activity observed off the Amazon shelf.

257 **3.2.1 Baroclinic tidal current**

258 The contribution of the ITs to the total baroclinic velocity structure is shown (Fig. 4a.1 to 4c.1, and Fig. A2.a.1 to A2.g.1,
259 Appendix) by the temporal evolution of the baroclinic tidal current. The semi-diurnal M2 component of the baroclinic current
260 is easily identified by alternating positive (red bands) and negative (blue bands) velocities along T1-T4. For the IN-ITs stations
261 (Fig. 4a.1 to 4c.1, and Fig. A2.a.1 to A2.f.1, Appendix), M2 component signal is strong between depths of 100-300 m (e.g., at
262 S10-S14) and 100-400 m (e.g., at S6) and 200-450 m (e.g., at S21). Whereas the signal is noisier at depth for OUT-ITs stations
263 (e.g., at S24) along T5 (Fig. A2.g.1, Appendix). The baroclinic tidal velocity shows a superposition of several (03-05) tidal
264 modes. A high number of modes are observed on the shelf-break (e.g., 04 modes at S6 and 05 modes at S10). While a low
265 number of modes away from the shelf-break (e.g., 03 modes at S7, S12 and S14). The highest baroclinic tidal current velocities
266 were observed (between 25 - 48 cm.s^{-1}) at sites Aa and Ab along T1-T2. Whereas lower tidal velocities (< 25 cm.s^{-1}) are found
267 in site F along T4 (e.g., at S20 and S21) compared to OUT-ITs stations (e.g., at S24). The strong vertical shears ($> 10^{-3}$ s^{-2}) of

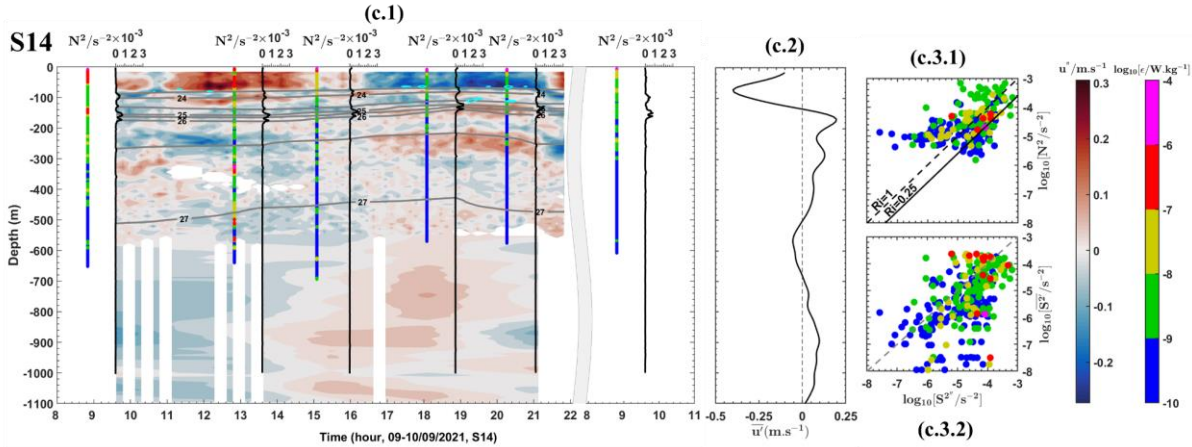


268 the baroclinic tidal velocities are clearly localized in the pycnocline (between 80-180 m depth) for the IN-ITs stations (e.g., at
269 S6, S10 and S12). While weak vertical tidal shears ($< 10^{-3} \text{ s}^{-2}$) are observed at greater depths. At these stations (e.g., S6, S10
270 and S14), the large vertical displacements of maximum N^2 were also encountered in pycnocline over tidal period. The
271 dissipation rates (ϵ) already presented in section 3.1.2, is also reported on Fig. 3. ϵ shown over the tidal period at long stations
272 (e.g., at S6, S10 and S14) are found 2-3 orders of magnitude stronger in the pycnocline than at depth.



273

274



275

276

277

278

279

280

281

282

283

284

285

286

287

288

289

290

291

292

293

294

295

296

297

298

Figure 4: (1st column: a.1 to c.1) Semi-diurnal (u'' in $m.s^{-1}$) baroclinic zonal currents from ADCP overlaid the semi-diurnal vertical shear squared ($S^{2''}$ in $s^{-2} \times 10^{-3}$ with the following contours values: 1.2 at S10, 0.6 at S11 and 0.8 at S14, in cyan contours) from ADCP, the buoyancy frequency squared (N^2 in s^{-2} , in vertical black lines) and potential density (in grey contours background shift) from CTD- O_2 and dissipation rates (ϵ in $W.kg^{-1}$ on log scale, in coloured bars) profiles from VMP. (2nd column: a.2 to c.2) Mean baroclinic (alongshore current) velocity (\bar{u}' in $m.s^{-1}$) from ADCP. (3rd column: a.3.1 to c.3.1) ϵ as a function of $S^{2''}$ and N^2 overlaid Richardson number (with critical value $Ri=0.25$ in solid black line and $Ri=1$ in dashed black line). (3rd column: a.3.2 to c.3.2) ϵ as function of mean vertical shear squared ($\bar{S}^{2'}$ in s^{-2}) and $S^{2''}$ overlaid dashed grey line for comparison. (first line, panels a) for S10, (second line, panels b) for S11 and (third line, panels c) for S14. N^2 was linearly interpolated into the depths of $S^{2''}$ to have same vertical scales.

3.2.2 Mean baroclinic current

Now, the contribution of the mean baroclinic current is diagnosed by the alongshore baroclinic velocities (taken parallel to the 200 m depth isobath) as a proxy of the main circulation pattern in the region. A surface alongshore northwestward flow crossing transects T1 and T2 (e.g., at S6, S7, and S10-S14) is observed stronger with mean (negative) velocities exceeding $40 cm.s^{-1}$ in the upper layer of 120 m (Fig. 4a.2 to 4c.2, and Fig. A2.a.2 to A2.d.2, Appendix). It moves with decreasing velocities towards the subsurface layer. Below 130 m depth on these transects (T1 and T2), a flow with relatively low (positive) velocities ($\sim 25 cm.s^{-1}$) is observed towards the southeast. In this layer, there are extremes of (positive) velocities (e.g., at S10, S11 and S13) and also direction reversals below 300 m (e.g., at S13 and S14). In contrast, a surface flow crossing T4 (Fig. A2.e.2 and A2.f.2, Appendix) is found moving southeastward in the first 100 meters depth. It shows mean (positive) velocities up to $35 cm.s^{-1}$ (e.g., at S20) before decreasing in the subsurface layer. Below 100 m depth, a flow northwestward is observed on T4 and rapidly becomes unstable (e.g., at S21). In this layer, there is a reversal of direction and low flow velocities ($< 15 cm.s^{-1}$) towards the depths. For OUT-ITs T5 transect (e.g., at S24), a bidirectional flow is observed moving southeastward at the surface and northwestward in the subsurface layer with low ($< 15 cm.s^{-1}$) mean velocities (Fig. A2.g.2, Appendix).



299

300 3.2.3 Competitive processes to generate mixing

301 Our intention is now to clearly associate each mixing event to either tides or mean currents. For that purpose we will compare
302 for each mixing event the vertical shear induced by the baroclinic tidal current ($S^{2''}$) to those induced by the baroclinic mean
303 current ($\overline{S^{2'}}$). Practically, each ε was analyzed in ($N^2, S^{2''}$) and ($\overline{S^{2'}}, S^{2''}$) space. The hotspots of ε are observed where there is
304 important vertical shear instability. Indeed, along T1-T2 and T4 (Fig. 4a.3.2 to 4c.3.2, and Fig. A2.a.3.2 to A2.g.3.2,
305 Appendix), strong mixing between [$10^{-8}, 10^{-5}$] W.kg $^{-1}$ on the IN-ITs transects (e.g., at S6, S10, S14 and S21) are found where
306 $S^{2''}$ is stronger (e.g., up to $1.4 \times 10^{-3} \text{ s}^{-2}$ at S6, $1.2 \times 10^{-3} \text{ s}^{-2}$ at S10 and $0.8 \times 10^{-3} \text{ s}^{-2}$ at S14) than $\overline{S^{2'}}$. Tidal vertical shear was
307 large enough to cross the large stratification (with N^2 up to 10^{-3} s^{-2} where $Ri < 0.25$) along T1 and T2 (Fig. 4a.3.1 to 4c.3.1,
308 and Fig. A2.a.3.1 to A2.d.3.1, Appendix). This was not true (with $Ri > 1$) where there are more ε between [$10^{-9}, 10^{-8}$] W.kg $^{-1}$
309 (e.g., at S20, S21 and S24) along T4 and T5 (Fig. A2.e.3.1 to A2.g.3.1, Appendix). Others mixing events within [$10^{-9}, 10^{-6}$]
310 W.kg $^{-1}$ were observed where $\overline{S^{2'}}$ is more relevant (up to 10^{-3} s^{-2}) than $S^{2''}$ or where there is low $S^{2''}$ shear (e.g., up to 0.4×10^{-3}
311 s^{-2} at S21).

312 To better clarify which of the tidal vs mean vertical shear is dominating to explain the hotspots of mixing, we compare the
313 contribution of the semi-diurnal ($\varepsilon''_{\text{MG}}$) and mean ($\overline{\varepsilon'}_{\text{MG}}$) baroclinic energy to the total baroclinic energy, by simply transforming
314 the vertical shear into turbulent energy (Table A1, Appendix). On T1 and T2, the contribution of $\varepsilon''_{\text{MG}}$ was found dominant
315 (61.2 % at S6 and 65.94 % at S10) compared with that (38.8 % at S6 and 34.06 % at S10) of $\overline{\varepsilon'}_{\text{MG}}$ on the IT generation on the
316 shelf-break. The same is true far from the shelf-break for some IN-ITs stations on T1 (e.g., at S12, S13 and S14) and on T4
317 (e.g., at S20 and S21). But this is not the case for other IN-ITs stations (e.g., at S7 and S11) where the contribution of $\varepsilon''_{\text{MG}}$
318 suddenly drops, and for OUT-ITs stations (e.g., at S24) where the contribution (> 50 %) of $\overline{\varepsilon'}_{\text{MG}}$ dominates. However, the
319 contribution of $\varepsilon''_{\text{MG}}$ increases (from 51.85 % at S12 to 58.94 % at S14) along T1, while it decreases (from 59.13 % at S21 to
320 52.64 % at S20) along T4. The contribution to the baroclinic energy supports the hypothesis that mixing is dominated by ITs
321 on the IT generation sites on the shelf-break, by mean circulation far IT fields, and both by ITs and background circulation
322 away from the shelf-break.

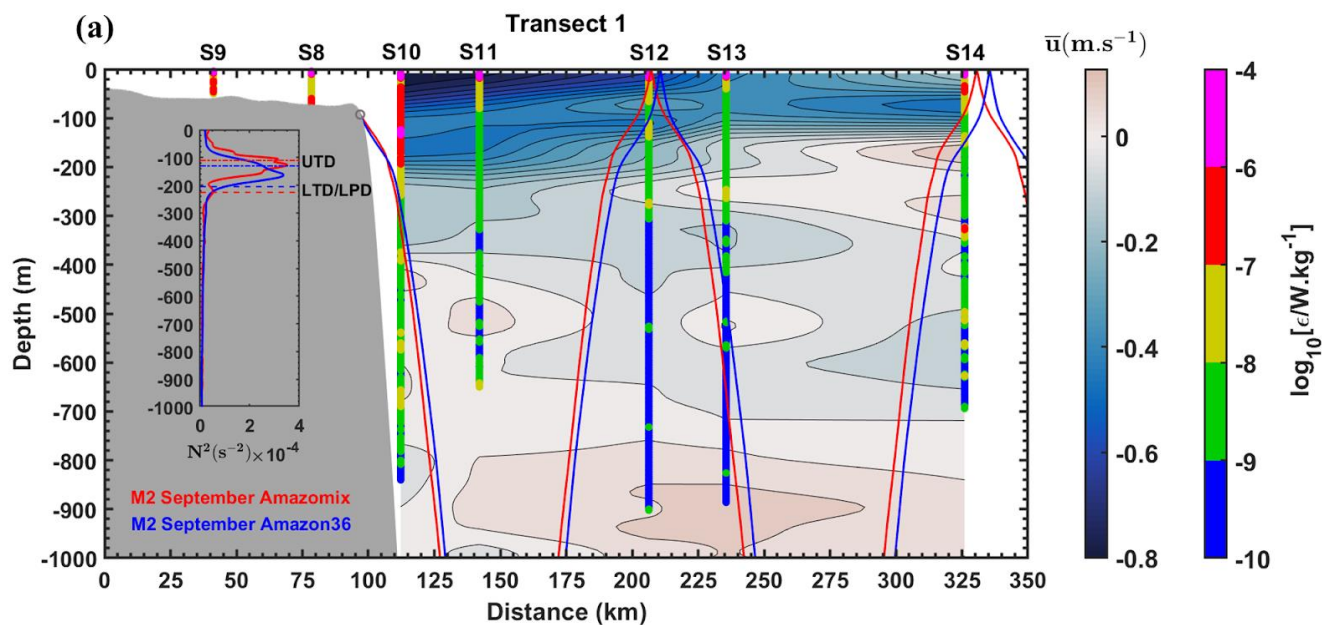
323

324 3.2.4 IT ray tracing

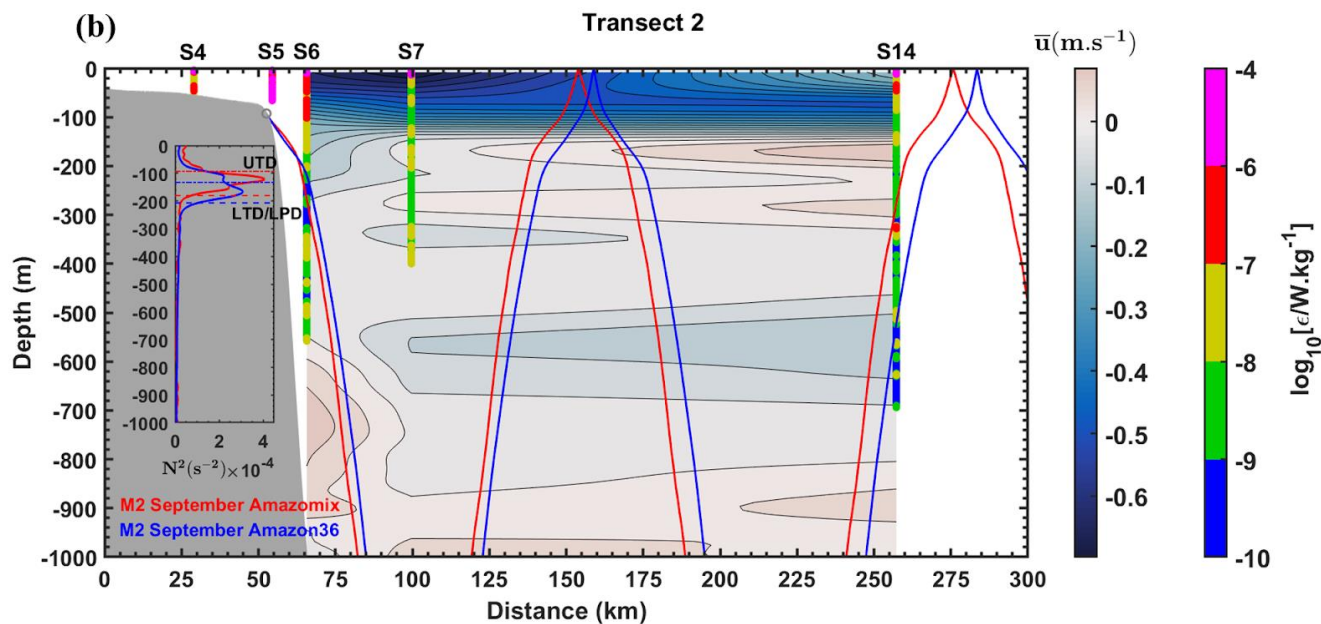
325 Another way of looking at the two main processes that can explain the mixing measured is to look at the vertical profiles of
326 the mean total (alongshore) currents, with the spatial dimension along the transect of IT rays propagation. IT ray paths are
327 computed for the M2 tidal frequency and the rays for September are illustrated along the ITs-IN transects T1-T4 (Fig. 5a and
328 5b, and Fig. A3.a to A3.e, Appendix). IT rays are generated at the critical slope (between 32-104 km from the coast) on
329 Amazon shelf-break, then propagate downward into the deep ocean where they reflect for the first time (within 1250-3900 m
330 depth and at a distance between 54-222 km, not shown). After bottom reflection and eventual interaction with the pycnocline,
331 IT ray paths were observed reflecting at the surface seaward at a distance of about 115-400 km (e.g., at T1-T4). The curvature



332 of the IT rays is more pronounced when they reach the pycnocline depths delimited (between 93-207 m depth at T1-T4) by
 333 the upper (UTD) and lower (LTD) thermocline depth. Along T1 and T2 (Fig. 5a and 5b), alongshore flow towards northwest
 334 is found stronger at the surface with a maximum (negative) velocity up to 80 cm.s^{-1} (e.g., at S11) above 150 m depth. This
 335 flow becomes unstable beyond 150-450 m depth. A flow instability was also observed along T4 (Fig. A3.e, Appendix). Large
 336 ϵ are encountered where IT rays paths presumably interfere either between them or with the mean flow (Fig. 5a and 5b).
 337 Tracking IT rays along the transects (Fig. 5a and 5b, and Fig. A3.a to A3.e, Appendix), ϵ are found larger (within $[10^{-8}, 10^{-5}]$
 338 W.kg^{-1}) in the rays generation (e.g., at S3, S5 and S10) and propagation (e.g., at S6 and S21). Some large ϵ are observed where
 339 IT rays radiated at the surface (e.g., at S12, S14 and S20) and below 300 m depth (at S14 along T1). These results indicate that
 340 turbulent dissipation occurred on the IT rays paths, and where rays interfere with each other and encounter the strong mean
 341 background circulation.



342



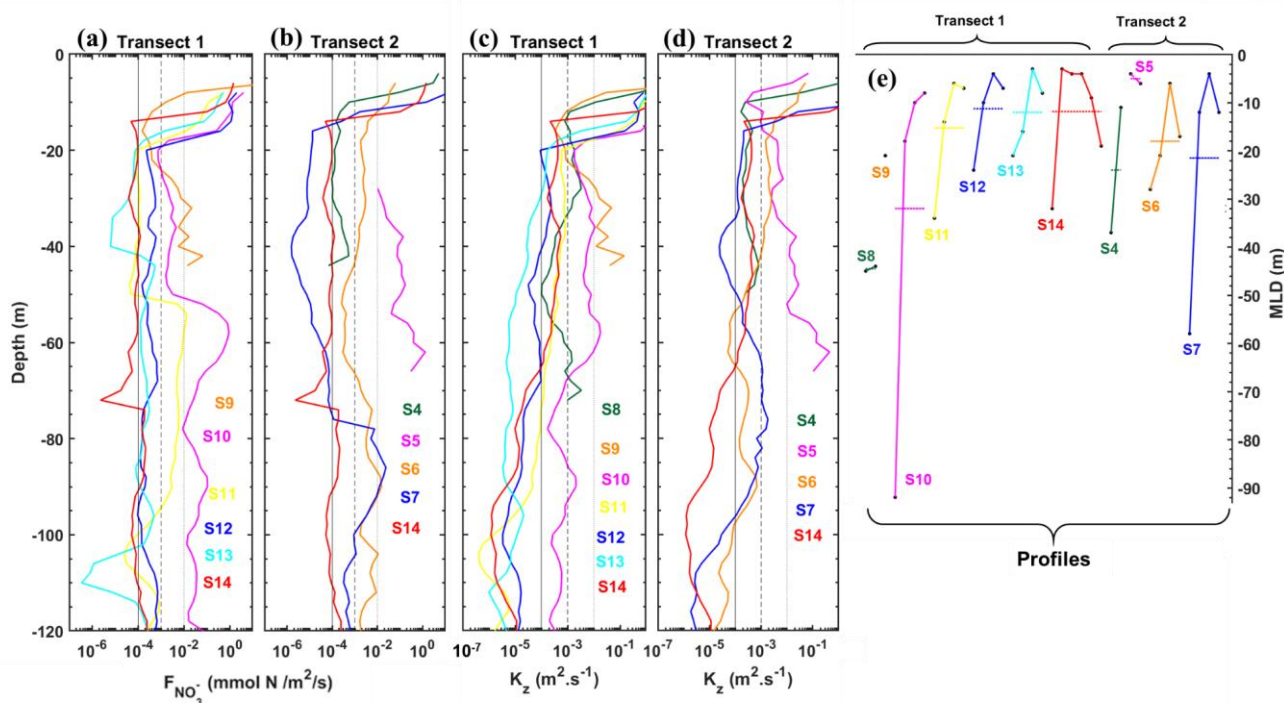
343
 344 Figure 5: Vertical sections showing: IT ray-tracing diagrams for the M2 tidal constituent assuming the mean (September)
 345 stratification (N^2 in s^{-2} , in overlaid panel) from AMAZOMIX CTD-O₂ (2021, in red line) and NEMO model (Amazon36, 2012-
 346 2016, in blue line), along the transects (a) T1 and (b) T2. Overlaid on the panels the profiles of dissipation rates (ϵ in $W \cdot kg^{-1}$
 347 on log scale, in coloured bars) from VMP, and the profiles of mean total (alongshore) current (\bar{u} in $m \cdot s^{-1}$, in background) for
 348 T1 and T2 from ADCP. UTD (in dotted lines) and LTD/LPD (in dashed lines) correspond to Upper and Lower
 349 Thermocline/Pycnocline Depth, respectively. Grey circles indicate the critical slope and grey areas represent local
 350 bathymetry.

351
 352 **3.3 Vertical diffusivity and nutrients flux at the base of the mixed layer**

353 The next steps of our study is dedicated to quantifying how much mixing could be responsible for nutrients uplift toward the
 354 euphotic layer, which may explains a boost in local primary production. Mixing coefficients were evaluated through vertical
 355 diffusivity (K_z). K_z is first analysed in the water column (Fig. A4, Appendix), and then at the base of MLD in Fig. 6c-e for T1
 356 and T2 (and on Fig. A6.c and A6.d for T3 to T5, Appendix). For IN-ITs stations on T1-T4 (Fig. A4, Appendix), K_z is higher
 357 between $[10^{-2}, 10^{-1}] m^2 \cdot s^{-1}$ in the mixed layers (e.g., at S10) and closer to the bottom layer. K_z is found smaller but still important
 358 below 200 m depth, with levels ranging between $[10^{-4}, 10^{-3}] m^2 \cdot s^{-1}$. For OUT-ITs stations on T5 (Fig. A4, Appendix), K_z
 359 remains stronger up to $10^{-4} m^2 \cdot s^{-1}$ below 200 m depth at S24, with two highest values exceeding $10^{-2} m^2 \cdot s^{-1}$ below XLD at S25.
 360 Finally, at the base of MLD, strong K_z is observed between $[10^{-3}, 10^{-0}] m^2 \cdot s^{-1}$ on the Amazon shelf (e.g., at S5 and S9) and the
 361 generation sites (e.g., at S3, S6, and S10), as well as within $[10^{-4}, 10^{-3}] m^2 \cdot s^{-1}$ along IT pathways. The question now is could it
 362 trigger a strong vertical flux of nutrients that may boost primary production? With simple consideration we calculate the



363 vertical flux of nutrients (nitrate and phosphate) at the base of MLD. Nitrate flux is analyzed in Fig. 6a-b for T1 and T2 (and
 364 in Fig. A6.a and A6.b for T3 to T5, Appendix).
 365 Nitrate fluxes at the base of MLD are higher within $[10^{-2}, 10^0]$ mmol N $m^{-2}.s^{-1}$ between 30-95 m depth along T1-T3 (e.g., at
 366 S2, S3, S5-S7, and S9-S11), and smaller but still large within $[10^{-3}, 10^{-2}]$ mmol N $m^{-2}.s^{-1}$ around 60-120 m depth on T4 (e.g.,
 367 at S19-S21). Other stations inside (e.g., S4, S12-S14) and outside (e.g., S24 and S25) of IT fields reveal nitrate fluxes even
 368 smaller approximately $[10^{-5}, 10^{-3}]$ mmol N $m^{-2}.s^{-1}$ at the base of MLD.
 369 Also, phosphate fluxes (Fig. A5, Appendix) at the base of MLD are stronger between $[10^{-3}, 10^{-1}]$ mmol P $m^{-2}.s^{-1}$ around 30-95
 370 m depth along T1-T3 (e.g., at S2, S3, S4, S5, S7 and S10), and smaller but still significant within $[10^{-4}, 10^{-3}]$ mmol P $m^{-2}.s^{-1}$
 371 between 60-120 m depth on T4 (e.g., at S19-S21). Phosphate fluxes along T4 are still smaller about $[10^{-6}, 10^{-4}]$ below the MLD
 372 and even exceeding 10^{-2} mmol P $m^{-2}.s^{-1}$ above the MLD at S25. Finally, phosphate fluxes are essentially similar in shape as
 373 nitrate fluxes, which is relevant because they both depend mainly on K_z profiles (e.g., Fig. A6, Appendix). This indicates that
 374 significant vertical flux of nutrients was found where there was strong vertical diffusivity at the base of the mixed layers off
 375 the Amazon shelf.



376
 377 *Figure 6: (a)-(b) Vertical fluxes of nitrate ($mmol\ N\ m^{-2}.s^{-1}$) and (c)-(d) vertical diffusivity (in $m^2.s^{-1}$) at the base of MLD (defined*
 378 *at the MLD + 1m) during AMAZOMIX 2021 cruise for the transects/stations inside of the IT fields (a)-(c) T1 (S10-S14) and*
 379 *(b)-(d) T2 (S4-S7 and S14). Dashed and solid back lines are for comparison. (e) MLD (in m) for each CTD-O₂/LADCP (black*
 380 *dots), and average values (colored horizontal dashed lines) for each station. Colour is used to distinguish each station in each*
 381 *transect. Vertical flux of nitrate was null at S8 because of null nitrate concentration gradient.*



382

383 **4 Discussion and Conclusion**

384 AMAZOMIX 2021 cruise delivered for the first time direct measurements of turbulent dissipation using a velocity
385 microstructure profiler VMP over several stations in and out of the IT influence that allow to study mixing in the Amazon
386 Shelf break and open ocean facing it. To catch a tidal cycle, the measurements of turbulent dissipation rate, hydrography and
387 currents, and also nutrient concentrations were collected alternately during 12h with 4 to 5 profiles for each station (see section
388 2). The position of 12h stations were chosen using modeling results that provide realistic maps of ITs generation and
389 propagation (Fig. 1a; Tchilibou et al., 2022). Stations within IT influence were localized on the most energetics IT generation
390 regions in sites Aa, Ab and D (S6, S10 and S3) as referenced by previous studies (Magalhaes et al., 2016; Tchilibou et al.,
391 2022; Assene et al., 2024) and along the IT propagation paths (S8-S9 and S11-S14 for site Ab). Also, a less energetic ITs site
392 was sampled, in site F (at S20 located in the generation and S21 in the offshore). In addition, other stations were localized on
393 the specific points (S5, S9 for sites Aa and Ab and S19 for site F) where IT beams may also climb the shelf-break just after
394 generation. Finally, as for stations on the shelf-break, AMAZOMIX cruise also sampled regions out of the IT fields (S24) and
395 in open ocean (S25).

396

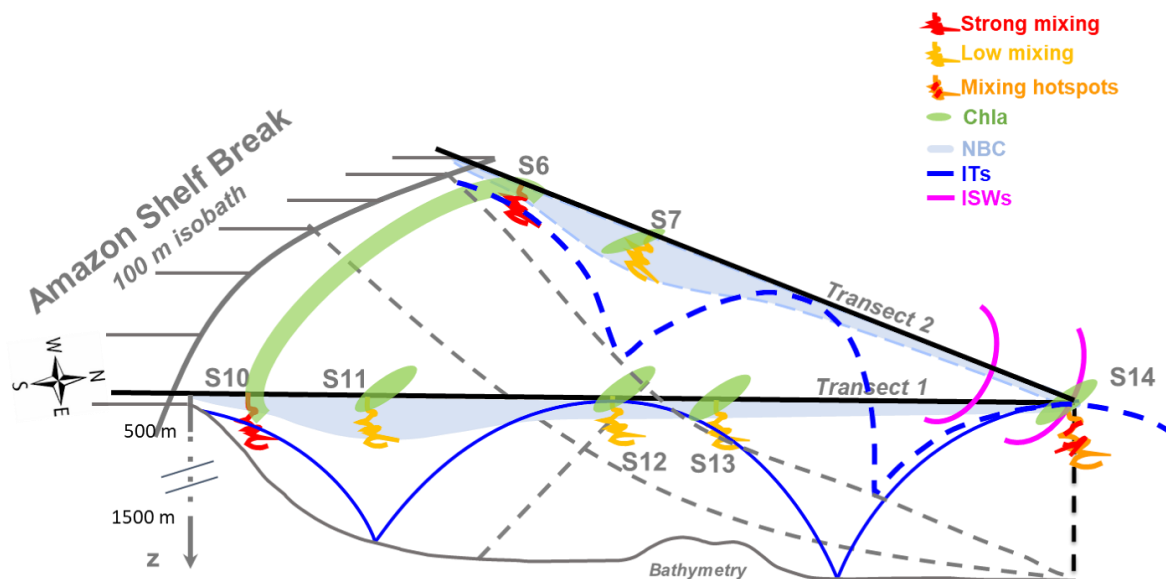
397 **Vertical Displacement, homogeneous layers**

398 The results showed that over a semi-diurnal tidal cycle, both large (up to 60 m length) isopycnal displacements and strong (up
399 to 40 m thick) step-like structures were found along the transects T1 and T2, whereas they are smaller and thinner on T3, T4
400 than T5. This is probably related to the propagation of ITs that produces vertical displacements at tidal frequency and
401 eventually mixing that creates homogeneous layers, identified on temperature and salinity structure as step-like features. We
402 found stronger energy along T1 and T2, compared to T3 and T4, as previously described by modeling studies (Tchilibou et
403 al., 2022; Assene et al., 2024). These step-like structures and isopycnal displacements in the pycnocline are also consistent
404 with the observations over a tidal cycle in other IT regions (Stansfield et al., 2001; Simpson and Sharples, 2012; Bordois, 2015;
405 Koch-Larrouy et al., 2015; Zhao et al., 2016; Bouruet-Aubertot et al., 2018; Xu et al., 2020).

406

407 **Direct measurements of dissipation rate**

408 Dissipation rates, obtained with the VMP, were stronger within $[10^{-6}, 10^{-4}]$ $W.kg^{-1}$ mainly on the generation sites Aa, Ab and
409 D (at S6, S10 and S3) and were smaller but still large $[10^{-9}, 10^{-7}]$ $W.kg^{-1}$ a few kilometers (~ 40 km) from these sites (at S2, S11
410 and S7), along the IT path (at S11-S13 and S20) and far IT fields (e.g., at S24). They were still higher between $[10^{-8}, 10^{-6}]$
411 $W.kg^{-1}$ in the open ocean mainly ~ 225 km from generation site Ab (at S14), as resumed in Fig. 7.



412
413 *Figure 7: Summary diagram showing the processes that lead to mixing along the AMAZOMIX transects (e.g., along T1 and*
414 *T2).*

415 In comparison, in other regions, dissipation rates measured by similar VMP instrument are found between $[10^{-7}, 10^{-5}] \text{ W.kg}^{-1}$
416 in the IT generation zone of Halmahera Sea, Indonesia (Koch-Larrouy et al., 2015; Bouruet-Aubertot et al., 2018), of Kaena
417 Ridge, Hawaii (Klymak et al., 2008) and off the Changjiang Estuary (Yang et al. 2020). Whereas it is $[10^{-10}, 10^{-8}] \text{ W.kg}^{-1}$ along
418 the IT path in the Southern Ocean (Gille et al., 2012) and in Halmahera Sea (Bouruet-Aubertot et al., 2018). Direct estimates
419 of dissipation far from IT influence are almost $[10^{-11}, 10^{-10}] \text{ W.kg}^{-1}$ (Koch-Larrouy et al., 2015; Bouruet-Aubertot et al., 2018)
420 or under the influence of geostrophic current (Takahashi and Hibiya, 2019).

421 Our study also found a very high dissipation rate for S3 and S5 of $[10^{-6}, 10^{-4}] \text{ W.kg}^{-1}$ on the Amazon shelf, increasing near the
422 bottom boundary layer. These findings compare well with values reaching $3 \times 10^{-9} \text{ W.kg}^{-1}$ within a kilometer of the seabed in
423 the Southern Ocean (Sheen et al., 2013) and up to $10^{-6} \text{ W.kg}^{-1}$ within a few meters from bottom topography off the Changjiang
424 Estuary (Yang et al. 2020). This may indicate the presence of an active bottom boundary layer. Thus, kinetic energy of bottom
425 flow was estimated using friction velocity, that was computed from total velocity averaged over the bottom-most 15 m for
426 shallow stations. It showed bottom friction energy stronger 9-22 J.m^{-2} at S3 and S5 mainly and lower ($< 1 \text{ J.m}^{-2}$) in the other
427 stations (e.g., at S8) on shelf. These results are smaller but still important on the Amazon shelf and comparable to values (5-
428 17 kJ.m^{-2}) in the Drake Passage region (on the continental slope) of the Southern Ocean (Laurent et al., 2012). The bottom
429 mixing at S3 and S5 can indirectly exert a control on pycnocline mixing on the Amazon shelf (Inall et al., 2021).

430
431
432



433 **Contribution of Background circulation and ITs to mixing**

434

435 **Mean baroclinic current shear**

436 Another important issue raised in this study was the quantification of the contribution of each process that could explain this
437 heterogeneous mixing.

438 Firstly, we considered the mean baroclinic current (BC) as a proxy of the background circulation. BC was mainly structured
439 in northwestward surface and southeastward subsurface flow. The strong surface flow (e.g., at S11) toward northwest is
440 associated with NBC originating from the northeast coast of Brazil (e.g., Bourlès et al., 1999). The subsurface flow (e.g., at
441 S11) toward southeast could be associated with the instability of the NBC in depth (Dossa et al., 2024; in preparation). Both
442 baroclinic flows were unstable and produced vertical shear instabilities stronger $>10^{-4} \text{ s}^{-2}$ at 100-120 m for NBC and $\sim 0.5 \times$
443 10^{-4} s^{-2} at 530-550 m for the subsurface flow at S7 and S11 mainly, while they were still larger ($>10^{-4} \text{ s}^{-2}$) above 80 m for NBC
444 at S6, S12-S14.

445 Other large shear instability of the mean current $> 2.5 \times 10^{-4} \text{ s}^{-2}$, located in NBC pattern at S20 could be associated with NBC
446 retroflexion around $5\text{-}6^{\circ}\text{N}$ during fall near 50°W (Didden and Schott, 1993). Finally, BC shear was $\sim 0.8 \times 10^{-4} \text{ s}^{-2}$ between
447 100-120 m at S21 and 40-60 m at S24 out the IT fields, and inside of the outer path of the Amazon plume. It is probably related
448 to the AWL from the continental inputs (Prestes et al., 2018) at S21 and S24, or due to the possible presence of subsurface
449 eddy at S21. This shows the potential of the mean flow to develop shear instability off the Amazon shelf.

450

451 **ITs shear**

452 Second, regarding IT, the baroclinic tidal currents, were separated from the total baroclinic currents, and showed significant
453 M2 semi-diurnal component signals, with high tidal modes 03-05 modes on the generations sites (S6 for Aa and S10 for Ab)
454 and on the IT path coming from sites Ab in S14), with strong vertical shear instabilities associated to it. These high modes
455 semi-diurnal baroclinic currents induced vertical tidal shears in the pycnocline layer (between 80-120 m). That was stronger
456 between $1.5\text{-}2 \times 10^{-3} \text{ s}^{-2}$ in the generation areas (S6 and S10), still larger $1\text{-}1.5 \times 10^{-3} \text{ s}^{-2}$ a few kilometers from generation sites
457 (S7 and S12) and smaller within $0.5\text{-}1 \times 10^{-3} \text{ s}^{-2}$ in the open ocean (e.g., at S20). Finally, for the stations out of the IT fields,
458 IT shear was $<10^{-3} \text{ s}^{-2}$ at S24 in the water column, but higher than that close to the bottom topography probably due to the
459 active bottom boundary layer (Inall et al., 2021).

460

461 **IT/BC ratio**

462 Each of IT and BC shear contributes to mixing. The ratio changes from one site to another: in the vicinity of the ITs generation
463 sites on the shelf-break, ITs dominated this ratio with $\sim 65\%/ \sim 35\%$ for IT/BC respectively (for S10). Also, it was about
464 $\sim 60\%/ \sim 40\%$ at S14 where IT beams from Aa and Ab encounter and may interfere.

465 Whereas along the A path, where NBC was strong at S11-S12, it was $\sim 50\%/ \sim 50\%$ and $\sim 55\%/ \sim 45\%$ at S13. This relative
466 diminution of IT influences compared to NBC may come from the fact that NBC was stronger at these stations.



467 Finally, for stations far from IT fields, BC dominated this ratio with ~49.6%/~50.4% at S24 due to both NBC and AWL.
468 These results are in good agreement with previous studies that showed strong tidal shear in the generation sites, such as in
469 Halmahera Sea (Bouruet-Aubertot et al., 2018), off the Changjiang Estuary (Yang et al. 2020), in the northwest European
470 continental shelf seas (Rippeth et al., 2005) or in the southern Yellow Sea (Xu et al., 2020).
471 The really new aspect raised in this study was the very large mixing found up to 225 km from generation sites, after the
472 reflection beams in S14 (Fig. 4), induced by strong tidal shears between $1-1.5 \times 10^{-3} \text{ s}^{-2}$ located above (60-80 m) and within
473 the pycnocline layer.

474

475 **Discussion on the strong mixing at S14**

476 Along IT paths, the higher remote dissipation rates (within $[10^{-7}, 10^{-6}] \text{ W.kg}^{-1}$) were found ~225 km from the shelf-break (S14).
477 Indeed, S14 experiences stronger mixing than S12 and S13. This region has been described by realistic models as a region of
478 strong dissipation of IT (Tchilibou et al., 2022; Assene et al. 2024). Also a recent satellite study, mapping ISWs generated
479 from ITs using MODIS images, showed that this region is also the region of higher occurrences of ISWs (de Macedo et al.,
480 2023). S14 is indeed localized where the ITs rays from Aa and Ab may intersect. It is also the region where the NBC vanishes.
481 Such change in the wave guide as well as the wave-wave interferences may generate the higher modes found. These higher
482 modes may in turn favor the generation of non-linear ISWs and higher dissipation rates found in this region. In addition, when
483 ITs disintegrate into a package of ISWs events (Jackson et al., 2012) they can lead to enhancing turbulent mixing (Xie et al
484 2013).

485 It should be noted that ITs interactions with baroclinic eddies could also lead to the turbulent dissipation (Booth and
486 Kamenkovich, 2008), in particular in this region of high eddy activities. However, no repeated AMAZOMIX stations
487 investigated here over a tidal period were observed to be enclosed by mesoscale eddy activity off the Amazon shelf, except
488 around S20-S21 where a possible subsurface eddy was detected.

489 Further study is necessary to better understand the complex interaction between all these processes, and AMAZOMIX data
490 will serve as a guide for future understanding and parameterization for modeling study.

491

492 **Role of mixing in nutrient fluxes off the Amazon shelf**

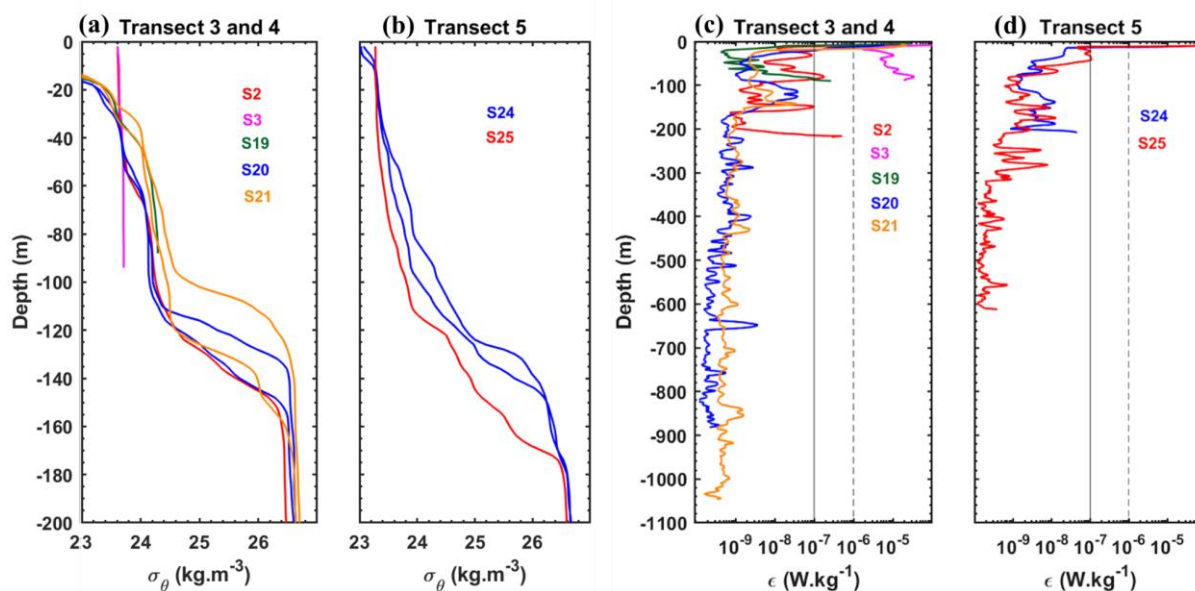
493 One last important aspect that we investigate in this study, is the impact of mixing on nutrient fluxes at the base of MLD.
494 Vertical fluxes of nitrate and phosphate were stronger around $[10^{-2}, 10^0] \text{ mmol N m}^{-2}.\text{s}^{-1}$ and $[10^{-2}, 10^0] \text{ mmol P m}^{-2}.\text{s}^{-1}$,
495 respectively, mainly on the generation sites Ab and D (e.g., at S10 and S3; Figure 6) where the vertical diffusivity was stronger
496 ($[10^{-3}, 10^{-1}] \text{ m}^2.\text{s}^{-1}$). They were smaller but still large between $[10^{-3}, 10^{-2}] \text{ mmol N m}^{-2}.\text{s}^{-1}$ and $[10^{-4}, 10^{-3}] \text{ mmol P m}^{-2}.\text{s}^{-1}$ a few
497 kilometers (~40 km) from these sites (at S11 and S7). The nitrate and phosphate fluxes were still smaller within $[10^{-4}, 10^{-3}]$
498 $\text{mmol N m}^{-2}.\text{s}^{-1}$ and $<10^{-4} \text{ mmol P m}^{-2}.\text{s}^{-1}$ along the IT path (at S12-S14 and S20) and far IT fields (e.g., at S24). Finally, they
499 were even larger around $[10^{-3}, 10^0] \text{ mmol N m}^{-2}.\text{s}^{-1}$ and $[10^{-3}, 10^0] \text{ mmol P m}^{-2}.\text{s}^{-1}$ on the Amazon shelf (e.g., at S5) where the
500 vertical diffusivity was stronger ($[10^{-3}, 10^0] \text{ m}^2.\text{s}^{-1}$).



501 Such diffusivity is consistent with the estimates of Koch-Larrouy et al. (2015) in the Indonesian seas, that also measured an
 502 impact on nutrient fluxes and associated chlorophyll primary production (Zaron et al. 2023).
 503 Tidal vertical diffusivity was also shown close enough to the surface to modify the heat content off the Amazon shelf (e.g.,
 504 Assene et al. 2024). Due to the shallow euphotic zone in this region, the strong upward fluxes of nitrate and phosphate may
 505 contribute in the surface layer to the local chlorophyll bloom off the Amazon shelf. The significant impact of the latter was
 506 highlighted and shown: an increase in chlorophyll concentration ($0.02\text{-}0.04\text{ mg.m}^{-3}$) using simple calculation, from glider and
 507 ocean color (M’Hamdi et al., 2024; in preparation), and from MODIS Terra sunglint images with and without ISWs events
 508 (de Macedo et al., 2023) off the Amazon shelf. The increase (1-2 orders of magnitude) in nutrient fluxes confirms the theory
 509 that mean supply of nutrients are often dominated by relevant IT mixing (Sharples and Zeldis, 2019; Kaneko et al., 2021; Yang
 510 et al., 2020). This finding implies that, in the AMAZOMIX region, ITs act as an important supplier of nutrient into the euphotic
 511 layer, able to maintain new primary production and to possibly impact the whole ecosystem.

512

513 **Appendices**



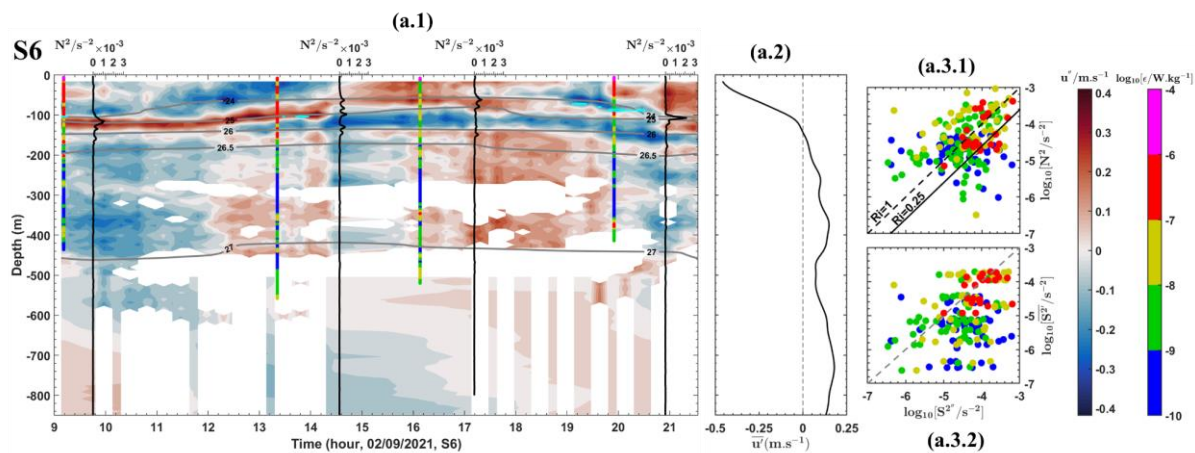
514

515 *Figure A1: (a)-(b) Potential density profiles (in kg.m^{-3}) from CTD- O_2 and (c)-(d) vertical dissipation rates (ϵ in W.kg^{-1} , on log
 516 scale) from VMP during the AMAZOMIX 2021 cruise for the transects/stations inside of the IT fields (a)-(c) T3 (S2 and S3)
 517 and T4 (S19-S21), and far from IT fields (b)-(d) T5 (S24 and S25). For long stations (S20 and S21), two density profiles are
 518 used to illustrate the isopycnal vertical displacements along the transects. The potential density at S3 varies between 23.6-
 519 23.72 kg.m^{-3} . Color of profiles is used to distinguish each station in each transect.*

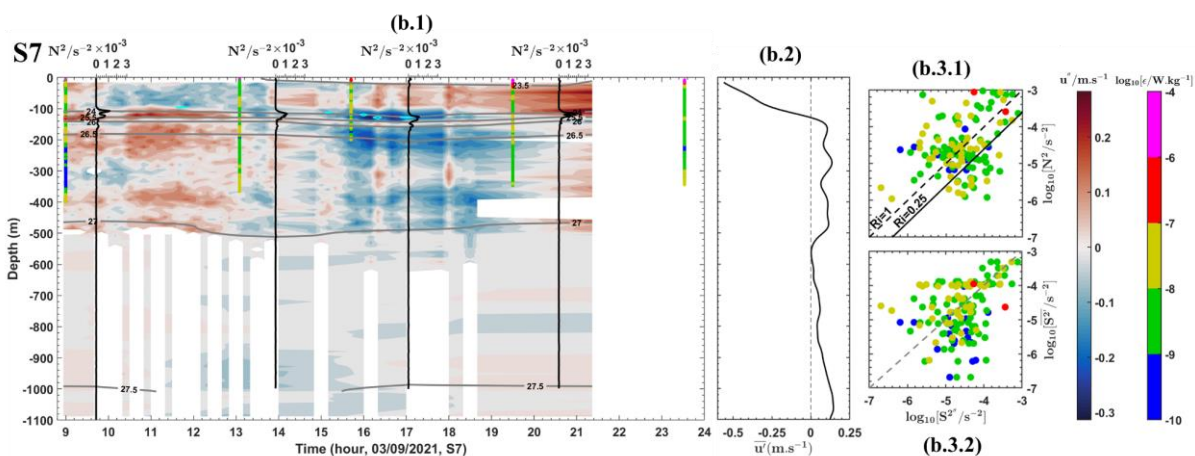
520



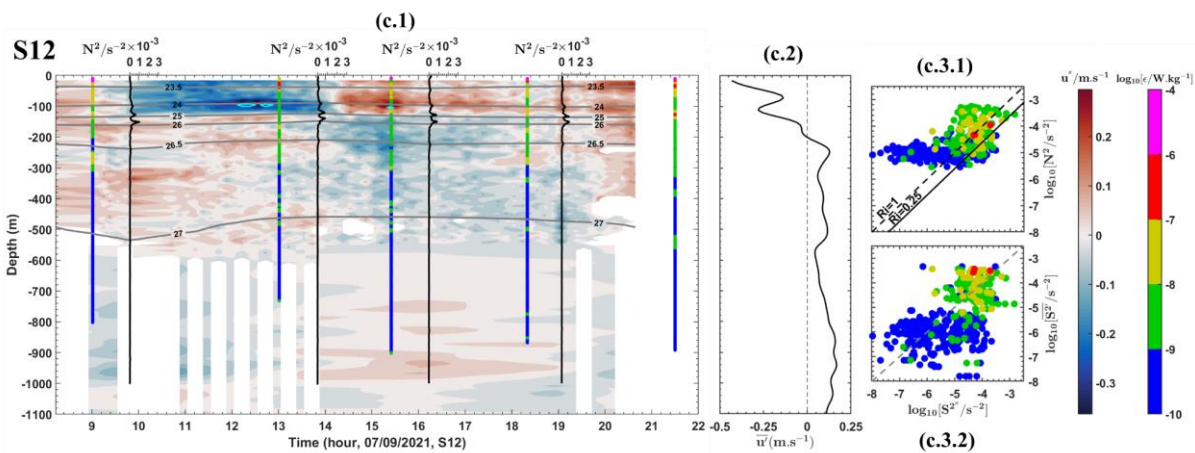
521



522

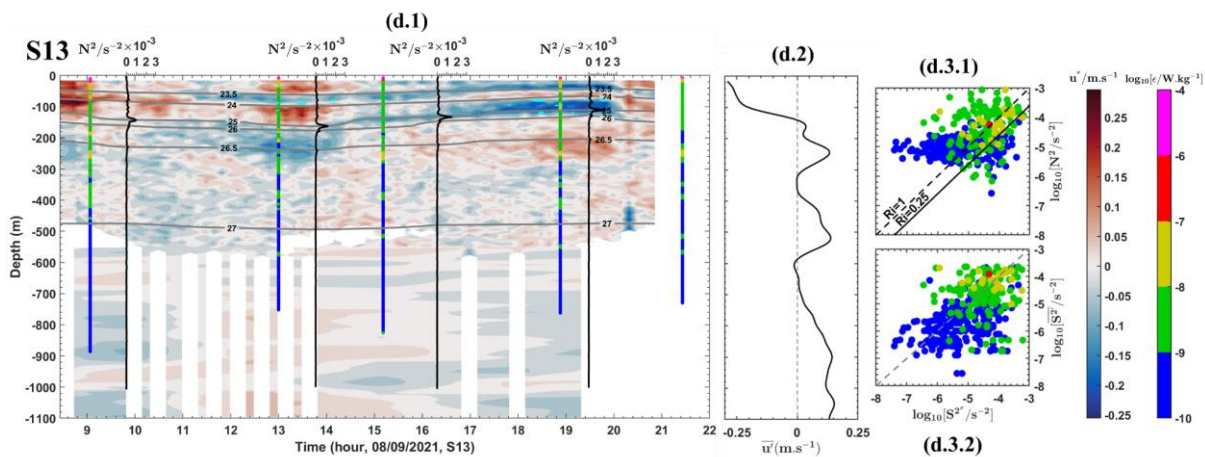


523

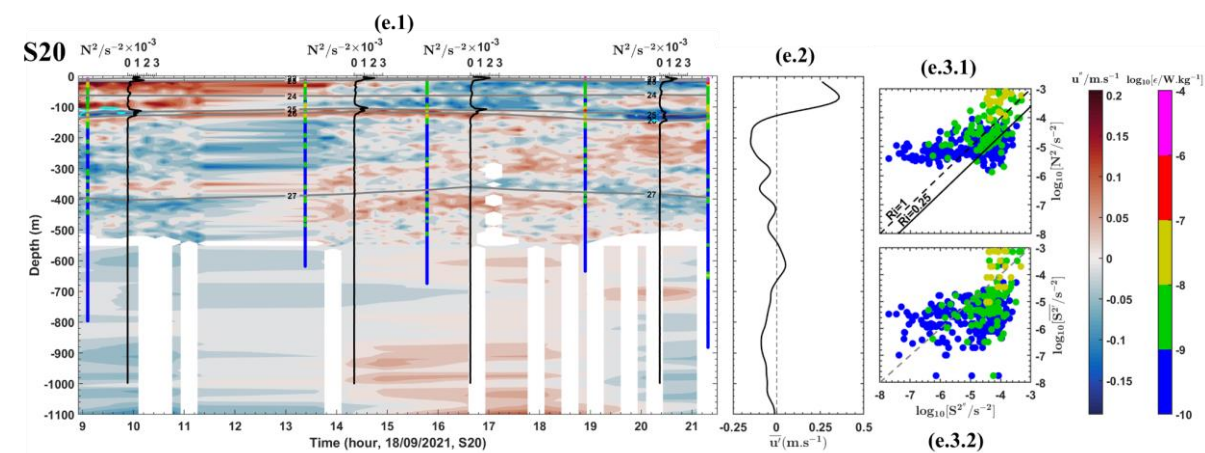




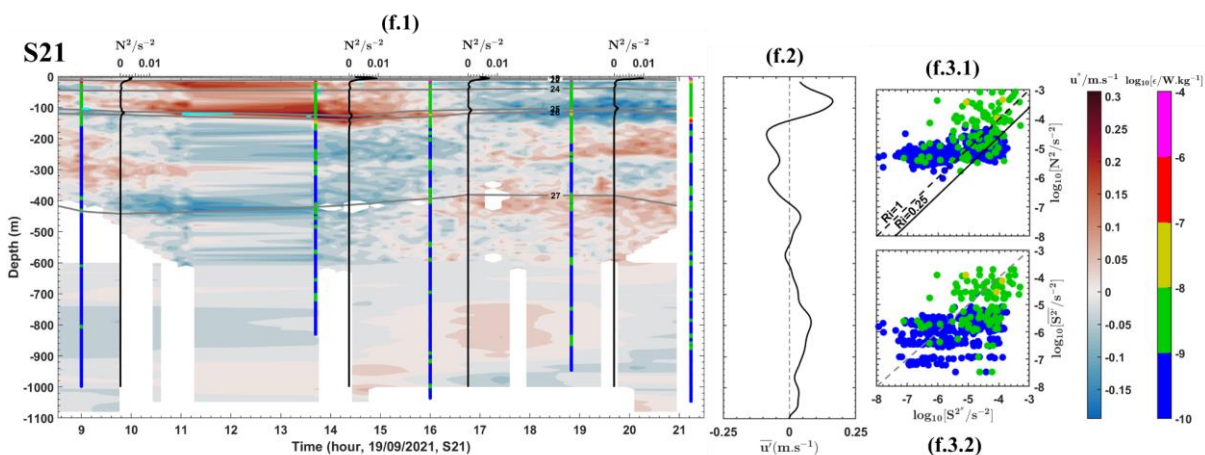
524

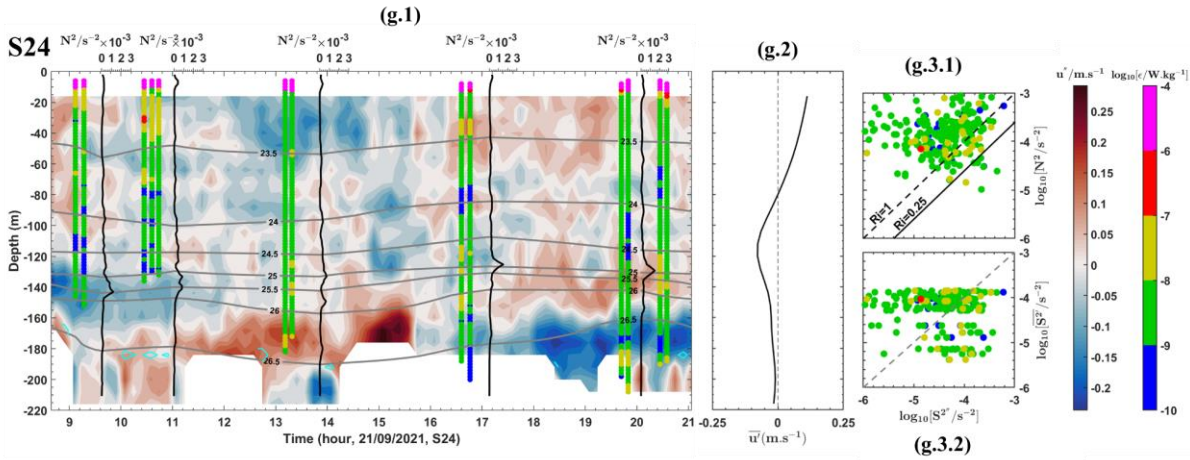


525



526





527

528

529

530

531

532

533

534

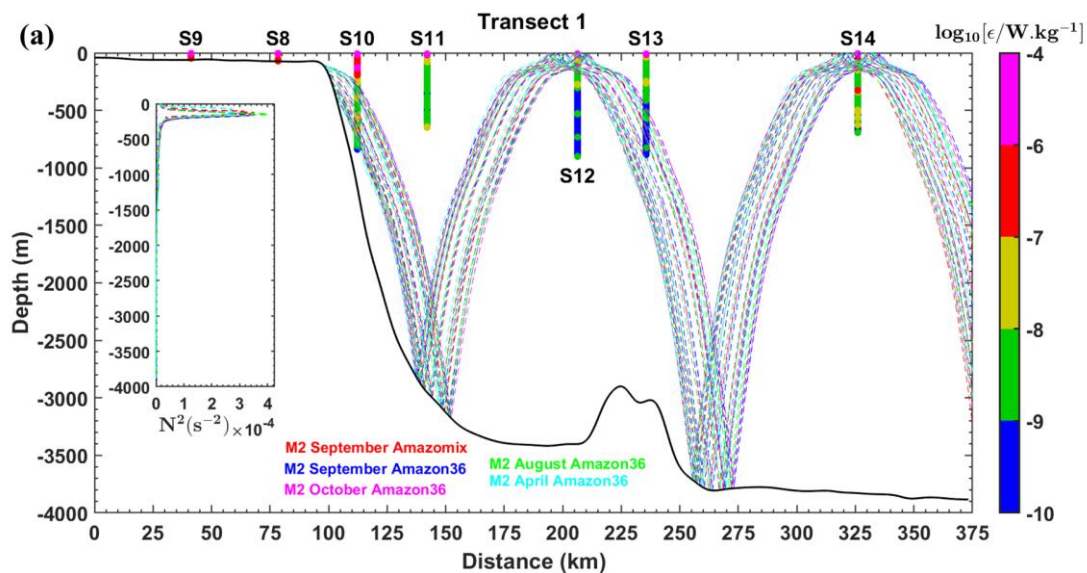
535

536

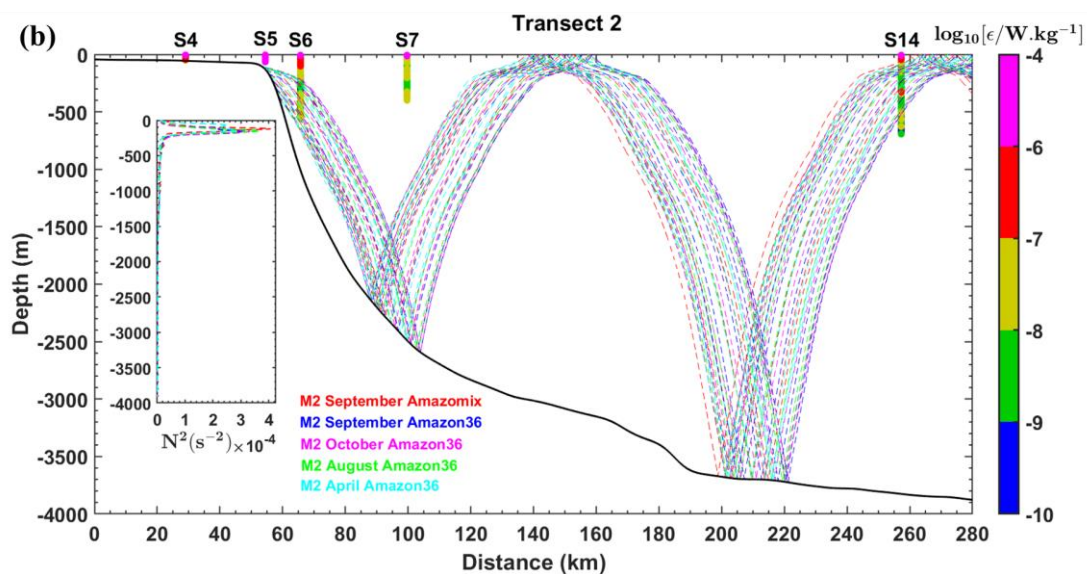
537

538

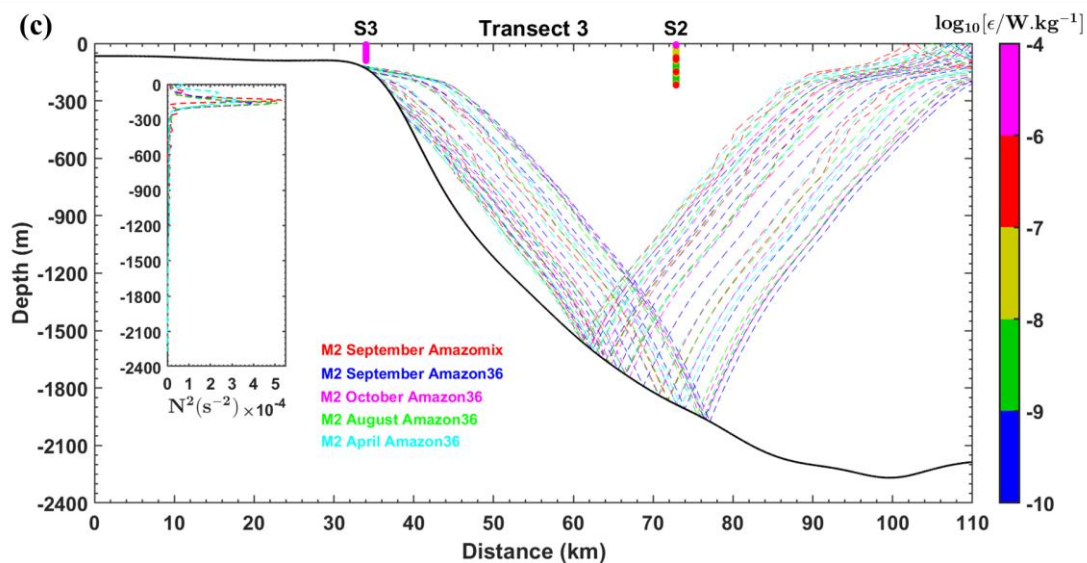
Figure A2: (1st column: a.1 to g.1) Semi-diurnal (u'' in $m.s^{-1}$) baroclinic zonal currents from ADCP overlaid the semi-diurnal vertical shear squared ($S^{2''}$ in $s^{-2} \times 10^{-3}$ with the following contours values: 1.4 at S6, 0.8 at S7, 1.1 at S12, 0.55 at S13, 0.5 at S20, 0.4 at S21 and 1.0 at S24, in cyan contours) from ADCP, the buoyancy frequency squared (N^2 in s^{-2} , in vertical black lines) and potential density (in grey contours background shift) from CTD- O_2 and dissipation rates (ϵ in $W.kg^{-1}$ on log scale, in coloured bars) profiles from VMP. (2nd column: a.2 to g.2) Baroclinic mean (alongshore current) velocity (\bar{u}' in $m.s^{-1}$) from ADCP. (3rd column: a.3.1 to g.3.1) ϵ as a function of $S^{2''}$ and N^2 overlaid Richardson number (with critical value $Ri = 0.25$ in solid black line and $Ri=1$ in dashed black line). (3rd column: a.3.2 to g.3.2) ϵ as function of mean vertical shear squared ($\overline{S^{2'}}$ in s^{-2}) and $S^{2''}$ overlaid dashed grey line for comparison. (first line, panels a) for S6, (second line, panels b) for S7, (third line, panels c) for S12, (fourth line, panels d) for S13, (fifth line, panels e) for S20, (sixth line, panels f) for S21 and (seventh line, panels g) for S24. N^2 was linearly interpolated into the depths of $S^{2''}$ to have same vertical scales.



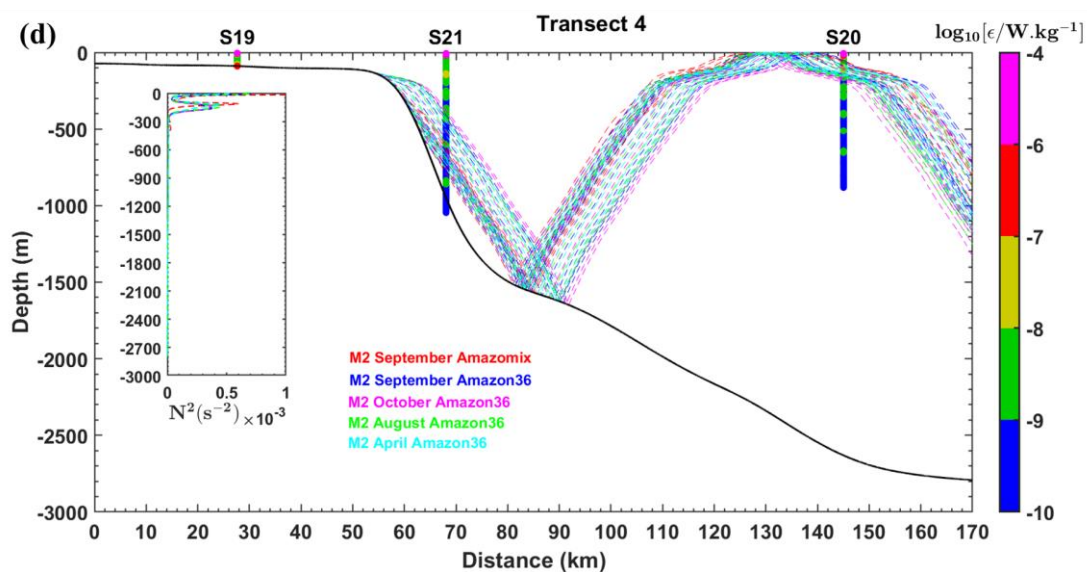
539



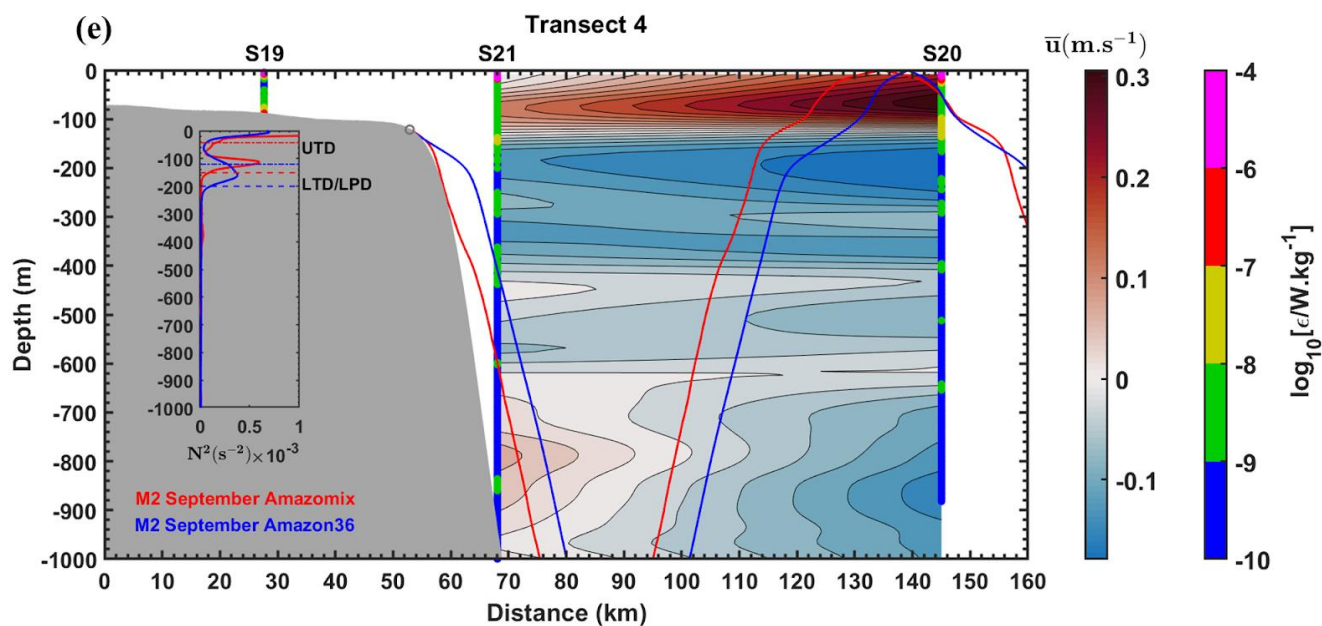
540



541



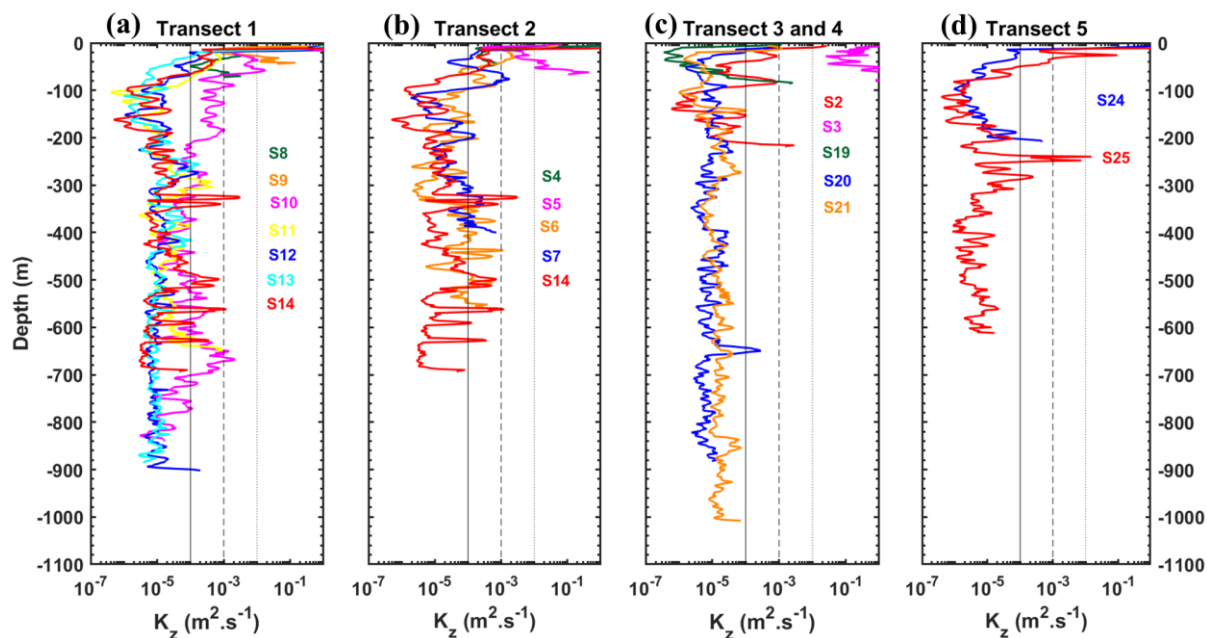
542



543

544 *Figure A3: (a)-(d) Sensibility tests of IT ray tracing by varying the location of the critical topography in each month. Ray*
 545 *tracing for the M2 tidal constituent assuming the mean stratification (N^2 in s^{-2} , in overlaid Figure in each panel) from*
 546 *AMAZOMIX CTD-O₂ (of September 2021) and NEMO model (Amazon36 of September, October, August and April, 2012-*
 547 *2016), along the transects (a) T1, (b) T2, (c) T3 and (d) T4. Overlaid on the panels the profiles of dissipation rates (ϵ in $W.kg^{-1}$*
 548 *in log scale, in coloured bars) from VMP. Solid black lines represent local bathymetry. Dashed colour lines are used to*
 549 *distinguish IT beam months in each transect. (e) Zoom in the upper layer of 1000 m at T4 showing IT ray tracing for September*
 550 *and the profiles of dissipation rates overlaid profiles of mean total (alongshore) current (\bar{u} in $m.s^{-1}$, in background) from*
 551 *ADCP. UTD (in dotted lines) and LTD/LPD (in dashed lines) correspond to Upper and Lower Thermocline/Pycnocline Depth,*
 552 *respectively. In the panel (e), grey circles indicate the critical slope and grey areas represent local bathymetry.*

553

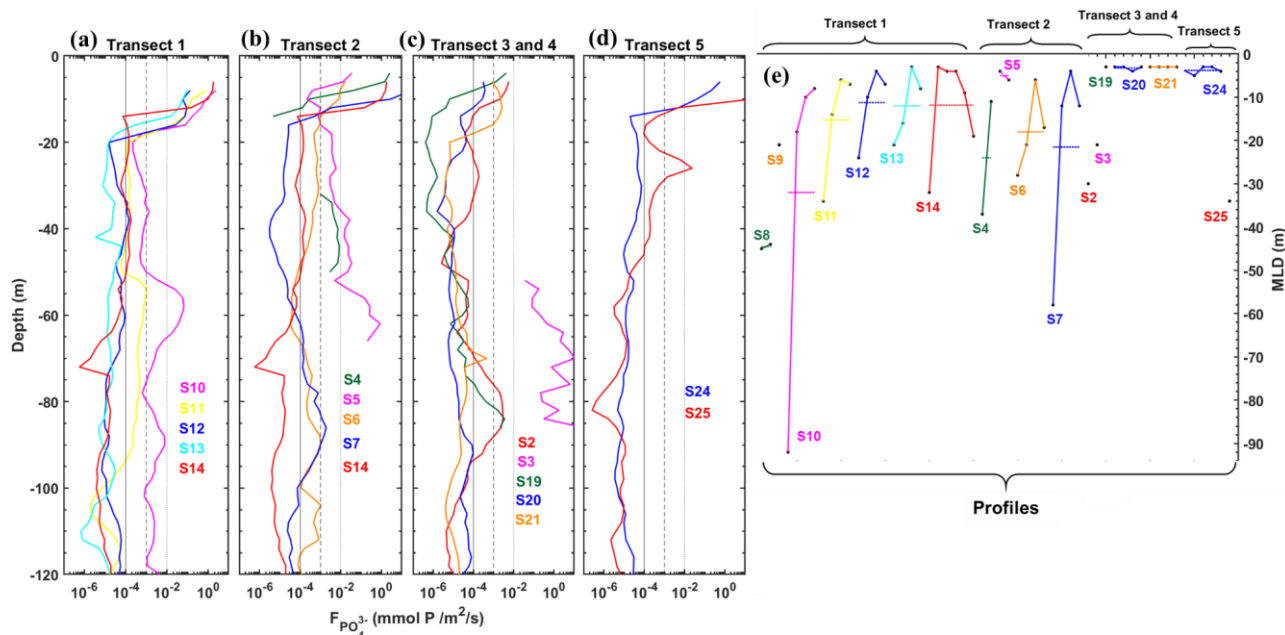


554

555 *Figure A4: Vertical diffusivity (in $m^2.s^{-1}$) during AMAZOMIX 2021 cruise for the transects/stations inside of the IT fields (a)*

556 *T1 (S8-S14), (b) T2 (S4-S7 and S14), and (c) T3 (S2 and S3) and T4 (S19-S21), and far from IT fields (d) T5 (S24 and S25).*

557 *Colour is used to distinguish each station in each transect. Dashed and solid back lines are for comparison.*



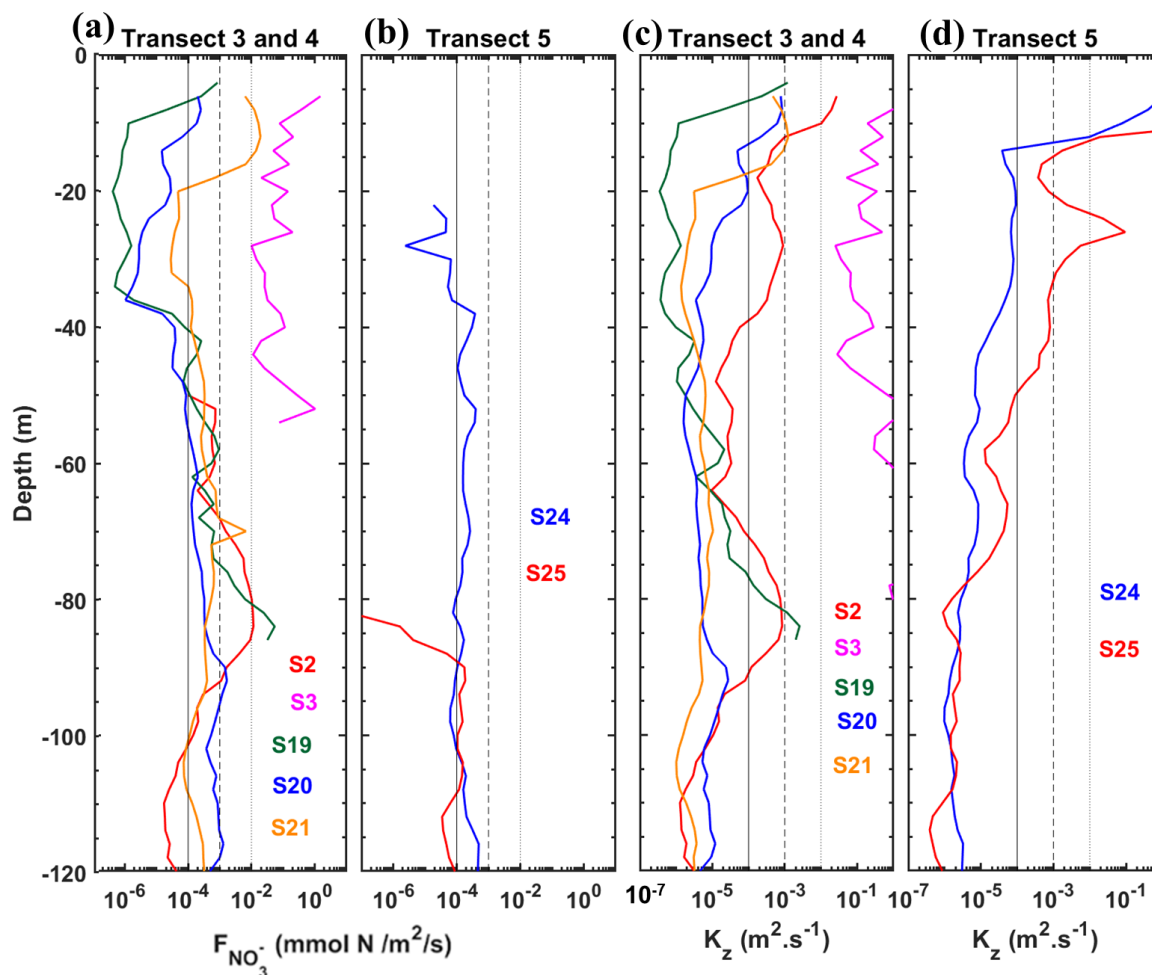
558

559 *Figure A5: Vertical fluxes of phosphate (in $mmol P m^{-2}.s^{-1}$) at the base of MLD (defined at the MLD + 1m) during AMAZOMIX*

560 *2021 cruise for the transects/stations inside of the IT fields (a) T1 (S10-S14), (b) T2 (S4-S7 and S14), and (c) T3 (S2 and S3)*



561 and T4 (S19-S21), and far from IT fields (d) T5 (S24 and S25). Dashed and solid back lines are for comparison. (e) MLD (in
 562 m) for each CTD-O₂ profile (black dots) with average values (horizontal dashed lines) for each station. Colour is used to
 563 distinguish each station in each transect. S9 was missing from the phosphate data and the vertical flux of phosphate was null
 564 at S8 because of null phosphate concentration gradient in Fig. A5.a.



565
 566 Figure A6: (a)-(b) Vertical fluxes of nitrate (in $\text{mmol N m}^{-2} \cdot \text{s}^{-1}$) and (c)-(d) vertical diffusivity (in $\text{m}^2 \cdot \text{s}^{-1}$) at the base of MLD
 567 (defined at the MLD + 1m, see Figure A5.e) during AMAZOMIX 2021 cruise for the transects/stations inside of the IT fields
 568 (a)-(c) T3 (S2 and S3) and T4 (S19-S21), and far from the IT fields (b)-(d) T5 (S24 and S25). Dashed and solid back lines are
 569 for comparison. Colour is used to distinguish each station in each transect.

570



571 *Table A1: miXing Layer Depth (XLD), Bottom layer-integrated flow Kinetic Energy (BKE), Contribution of the semi-diurnal*
 572 *(CSBE) and mean baroclinic (CMBE) energy to total baroclinic energy at AMAZOMIX stations. BKE was absent at stations*
 573 *with density stratification until the end of the profile.*

N°				
Stations	XLD (m)	BKE (J.m ⁻²)	CSBE (%)	CMBE (%)
S2	16	-	-	-
S3	16	22.94	-	-
S4	12	-	-	-
S5	8	9.52	-	-
S6	18	-	61.2	38.8
S7	44	-	48.38	51.62
S8	22	0.45	-	-
S9	14	1.32	-	-
S10	22	-	65.94	34.06
S11	18	-	48.07	51.93
S12	18	-	51.85	48.15
S13	18	-	56.03	43.97
S14	14	-	58.94	41.06
S19	24	0.56	-	-
S20	36	-	52.64	47.36
S21	36	-	59.13	40.87
S24	14	0.18	49.59	50.41
S25	12	-	-	-

574

575 **Data availability**

576 The AMAZOMIX data can be downloaded directly on the SEANOE site: <https://www.seanoe.org/data/00860/97235/>. The
 577 NEMOV3.6 model outputs are available upon request by contacting the corresponding author.

578

579 **Authors contributions**

580 AKL: funding acquisition. FK and AKL, with assistance from JM: conceptualization and methodology. FK, with assistance
 581 from PR, AB, EC and AKL: data pre-processing. Formal analysis: FK with interactions from all co-authors. Preparation of the
 582 manuscript: FK with contributions from all co-authors. This work is a contribution to the LMI TAPIOCA (www.tapioca.ird.fr).

583

584 **Competing interests**



585 The authors declare that they have no conflict of interest.

586

587 **Acknowledgments**

588 The authors would like to thank the “Flotte Océanographique Française” and the officers and crew of the R/V Antea for their
589 contribution to the success of the operations aboard the R/V ANTEA, as well as, all the scientists involved in data and water
590 samples collection, for their valuable support during and after the AMAZOMIX cruise. We acknowledge the Brazilian
591 authorities for authorising the survey. The authors acknowledge Rockland company for their instrument and their support
592 during the cruise and during the analysis of the VMP data, the National french parc of instrument (DT-INSU) for their
593 instrument during the cruise and support in data analysis, as well as, the US-IMAGO from IRD for its help during the cruise
594 and for biogeochemical data analysis.

595

596 **Financial support**

597 This work is a part of the project “AMAZOMIX”, funded multiple agencies : the “Flotte Océanographique Française” that
598 funded the 40 days at sea of the R/V Antea, the Institut de Recherche pour le Développement (IRD), via among other the LMI
599 TAPIOCA, the CNES, within the framework of the APR TOSCA MIAMAZ TOSCA project (PIs Ariane Koch-Larrouy,
600 Vincent Vantrepotte, and Isabelle Dadou), the LEGOS and the program international Franco-Brazileiro GUYAMAZON (call
601 N° 005/2017). It is also part of the PhD Thesis of Fabius Kouogang, funded by the Coordenação de Aperfeiçoamento de
602 Pessoal de Nível Superior (CAPES), under the co-advisement of Ariane Koch-Larrouy and Moacyr Araujo.

603

604 **References**

605 Araujo, M., Noriega, C., Hounsou-gbo, G. A., Veleda, D., Araujo, J., Bruto, L., Feitosa, F., Flores-Montes, M., Lefèvre, N.,
606 Melo, P., Otsuka, A., Travassos, K., Schwamborn, R., and Neumann-Leitão, S.: A Synoptic Assessment of the Amazon
607 River-Ocean Continuum during Boreal Autumn: From Physics to Plankton Communities and Carbon Flux, *Front.*
608 *Microbiol.*, 8:1358, <https://doi.org/10.3389/fmicb.2017.01358>, 2017.

609 Assene, F., Koch-Larrouy, A., Dadou, I., Tchilibou, M., Morvan, G., Chanut, J., Costa da Silva, A., Vantrepotte, V., Allain,
610 D., and Tran, T.-K.: Internal tides off the Amazon shelf – Part 1: The importance of the structuring of ocean temperature
611 during two contrasted seasons, *Ocean Sci.*, 20, 43–67, <https://doi.org/10.5194/os-20-43-2024>, 2024.

612 Assuncao, R. V., Silva, A. C., Roy, A., Bourlès, B., Silva, C. A. H. S., Ternon, J.-F., Araujo, M., and Bertrand, A.: 3D
613 characterisation of the thermohaline structure in the southwestern tropical Atlantic derived from functional data analysis
614 of in situ profiles, *Progress in Oceanography*, 187, pp.102399, <https://doi.org/10.1016/j.pocean.2020.102399>. hal-
615 02984588, 2020.



- 616 Barnier, B., Reynaud, T., Beckmann, A., Böning, C., Molines, J.-M., Barnard, S., and Jia, Y.: On the seasonal variability and
617 eddies in the North Brazil Current: insights from model intercomparison experiments, *Prog. Oceanogr.*, 48, 195–230,
618 [https://doi.org/10.1016/S0079-6611\(01\)00005-2](https://doi.org/10.1016/S0079-6611(01)00005-2), 2001.
- 619 Bertrand, A., de Saint Leger, E., and Koch-Larrouy, A.: AMAZOMIX 2021 cruise, RV Antea,
620 <https://doi.org/10.17600/18001364>, 2021.
- 621 Booth, J. and Kamenkovich, I.: Isolating the role of mesoscale eddies in mixing of a passive tracer in an eddy resolving model,
622 *J. Geophys. Res.*, 113, C05021, <https://doi.org/10.1029/2007JC004510>, 2008.
- 623 Bordois, L.: Internal tide modeling : Hydraulic & Topographic controls, Ph.D. thesis, Université Toulouse III Paul-Sabatier,
624 195 pp., tel-01281760, version 1., <https://theses.hal.science/tel-01281760>, 2015.
- 625 Bourlès, B., Gouriou, Y., and Chuchla, R.: On the circulation in the upper layer of the western equatorial Atlantic, *Journal of*
626 *Geophysical Research*, 104, 21151-21170, <https://doi.org/10.1029/1999JC900058>, 1999.
- 627 Bouruet-Aubertot, P., Cuyper, Y., Ferron, B., Dausse, D., Ménage, O., Atmadipoera, A. S., and Jaya, I.: Contrasted turbulence
628 intensities in the Indonesian Throughflow: a challenge for parameterizing energy dissipation rate, *Ocean Dynamics*, 68,
629 779–800, <https://doi.org/10.1007/s10236-018-1159-3>, 2018.
- 630 Didden, N. and Schott, F.: Eddies in the North Brazil Current retroflection region observed by Geosat altimetry, *J. Geophys.*
631 *Res.*, 98, 20121, <https://doi.org/10.1029/93JC01184>, 1993.
- 632 de Macedo, C. R., Koch-Larrouy, A., da Silva, J. C. B., Magalhães, J. M., Lentini, C. A. D., Tran, T. K., Rosa, M. C. B., and
633 Vantrepotte, V.: Spatial and temporal variability in mode-1 and mode-2 internal solitary waves from MODIS-Terra sun
634 glint off the Amazon shelf, *Ocean Sci.*, 19, 1357–1374, <https://doi.org/10.5194/os-19-1357-2023>, 2023.
- 635 Dossa, N., da Silva, A. C., Koch-Larrouy, A., and Kouogang, F.: Near-surface western boundary circulation off the Amazon
636 Plume from AMAZOMIX data, in preparation, 2024.
- 637 Fer, I., Dengler, M., Holtermann, P. et al.: ATOMIX benchmark datasets for dissipation rate measurements using shear probes,
638 *Sci Data*, 11, 518, <https://doi.org/10.1038/s41597-024-03323-y>, 2024.
- 639 Geyer, W. R.: Tide-induced mixing in the Amazon Frontal Zone, *J. Geophys. Res.*, 100, 2341,
640 <https://doi.org/10.1029/94JC02543>, 1995.



- 641 Gille, S.T., Ledwell, J., Naveira-Garabato, A., Speer, K., Balwada, D., Brearley, A., Garton, J.B., Griesel, A., Ferrari, R.,
642 Klocker, A., LaCasce, J., Lazarevich, P., Mackay, N., Meredith, M.P., Messias, M.-J., Owens, B., Sallée, J.-B., Sheen, K.,
643 Shuckburgh, E., Smeed, D. A., St. Laurent, L.C., Toole, J.M., Watson, A.J., Wienders, N., and Zajaczkovski, U.: The
644 diapycnal and isopycnal mixing experiment: a first assessment, *CLIVARExchanges*, 17(1), 46–48,
645 <https://nora.nerc.ac.uk/id/eprint/18245>, 2012.
- 646 Huang, P.-Q., Cen, X.-R., Lu, Y.-Z., Guo, S.-X., and Zhou, S.-Q.: Global distribution of the oceanic bottom mixed layer
647 thickness, *Geophysical Research Letters*, 46, 1547–1554, <https://doi.org/10.1029/2018GL081159>, (2019).
- 648 Huthnance, J. M.: Circulation, exchange and water masses at the ocean margin: the role of physical processes at the shelf edge,
649 *Progress in Oceanography*, 35, 353–431, [https://doi.org/10.1016/0079-6611\(95\)80003-C](https://doi.org/10.1016/0079-6611(95)80003-C), 1995.
- 650 Inall, M. E., Toberman, M., Polton, J. A., Palmer, M. R., Green, J. A. M., and Rippeth, T. P.: Shelf Seas Baroclinic Energy
651 Loss: Pycnocline Mixing and Bottom Boundary Layer Dissipation, *Journal of Geophysical Research: Oceans*,
652 126(8):2020JC016528, <https://doi.org/10.1029/2020JC016528>, 2021.
- 653 Ivey, G. N., Bluteau, C. E., Gayen, B., Jones, N. L., and Sohail, T.: Roles of Shear and Convection in Driving Mixing in the
654 Ocean, *Geophysical Research Letters*, 48(3), e2020GL089455, <https://doi.org/10.1029/2020GL089455>, 2021.
- 655 Jackson, C. R., da Silva, J. C. B., and Jeans, G.: The generation of nonlinear internal waves, *Oceanography*, 25(2):108–123,
656 <https://doi.org/10.5670/oceanog.2012.46>, 2012.
- 657 Johns, W. E., Lee, T. N., Beardsley, R. C., Candela, J., Limeburner, R., and Castro Filho, B. M. : Annual Cycle and Variability
658 of the North Brazil Current, *Journal of Physical Oceanography*, 28(1), 103-128, [https://doi.org/10.1175/1520-0485\(1998\)028%3C0103:acavot%3E2.0.co;2](https://doi.org/10.1175/1520-0485(1998)028%3C0103:acavot%3E2.0.co;2), 1998.
- 660 Kaneko, H., Yasuda, I., Itoh, S., and Ito, S.-I.: Vertical turbulent nitrate flux from direct measurements in the western subarctic
661 and subtropical gyres of the North Pacific, *J. Oceanogr.*, 77, 29–44, <https://doi.org/10.1007/s10872-020-00576-0>, 2021.
- 662 Koch-Larrouy, A., Atmadipoera, A., van Beek, P., Madec, G., Aucan, J., Lyard, F., Grelet, J., and Souhaut, M.: Estimates of
663 tidal mixing in the Indonesian archipelago from multidisciplinary INDOMIX in-situ data, *Deep Sea Research Part I: Oceanographic Research Papers*, 106, pp.136-153, <https://doi.org/10.1016/j.dsr.2015.09.007>, 2015.
- 665 Koch-Larrouy, A., Lengaigne, M., Terray, P., Madec, G., and Masson, S.: Tidal mixing in the Indonesian Seas and its effect
666 on the tropical climate system, *Clim. Dynam.*, 34, 891–904, <https://doi.org/10.1007/s00382-009-0642-4>, 2010.



- 667 Koch-Larrouy, A., Kerhervé, D., and Kouogang, F.: Evidence of overturns from AMAZOMIX off the Amazon shelf along
668 internal tides paths, in preparation, 2024.
- 669 Klymak, J. M., Pinkel, R., and Rainville, L.: Direct breaking of the internal tide near topography: Kaena ridge, hawaii, *J. Phys.*
670 *Oceanogr.*, 38 (2), 380–399, <https://doi.org/10.1175/2007JPO3728.1>, 2008.
- 671 Kunze, E.: The internal-wave-driven meridional overturning circulation, *J. Phys. Oceanogr.*, 47, 2673–2689,
672 <https://doi.org/10.1175/JPO-D-16-0142.1>, 2017.
- 673 Le Bars, M., Lacaze, L., Le Dizes, S., Le Gal, P., and Rieutord, M.: Tidal instability in stellar and planetary binary systems,
674 *Physics of the Earth and Planetary Interiors*, 178, 48-55, <https://doi.org/10.1016/j.pepi.2009.07.005>, 2010.
- 675 Lozovatsky, I. D., Roget, E., Fernando, H. J. S., Figueroa, M., and Shapovalov, S.: Sheared turbulence in a weakly stratified
676 upper ocean, *Deep Sea Res. Part I*, 53, 387–407, <https://doi.org/10.1016/j.dsr.2005.10.002>, 2006.
- 677 Lueck, R., Fer, I., Bluteau, C., Dengler, M., Holtermann, P., Inoue, R., LeBoyer, A., Nicholson, S., Schulz, K., and Stevens,
678 C.L.: Best practices recommendations for estimating dissipation rates from shear probes, *Frontiers in Marine Science*,
679 <https://doi.org/10.3389/fmars.2024.1334327>, 2024.
- 680 MacKinnon, J. A., and Gregg, M. C.: Mixing on the Late-Summer New England Shelf-Solibores, Shear, and Stratification,
681 *Journal of Physical Oceanography*, 33, 1476-1492, [https://doi.org/10.1175/1520-0485\(2003\)033<1476:MOTLNE>2.0.CO;2](https://doi.org/10.1175/1520-0485(2003)033<1476:MOTLNE>2.0.CO;2), 2003.
- 683 Madec, G., Bourdallé-Badie, R., Chanut, J., Clementi, E., Coward, A., Ethé, C., Iovino, D., Lea, D., Lévy, C., Lo-vato, T.,
684 Martin, N., Masson, S., Mocavero, S., Rousset, C., Storkey, D., Vancoppenolle, M., Müeller, S., Nurser, G., Bell, M., and
685 Samson, G.: NEMO ocean engine, Zenodo, <https://doi.org/10.5281/zenodo.3878122>, 2019.
- 686 Magalhaes, J. M., da Silva, J. C. B., Buijsman, M. C., and Garcia, C. A. E.: Effect of the North Equatorial Counter Current on
687 the generation and propagation of internal solitary waves off the Amazon shelf (SAR observations), *Ocean Sci.*, 12, 243–
688 255, <https://doi.org/10.5194/os-12-243-2016>, 2016.
- 689 M’hamdi, A., Koch-Larrouy, A., Bosse, A., de Macedo, C., Vantrepotte, V., Dadou, I., da Silva, A. C., and Kouogang, F.:
690 Internal tides imprints on chlorophyll in mesoscale intrathermocline lenses detected from ocean color and from in-situ
691 glider data off the Amazon shelf, *Ocean Sci.*, (in preparation), 2024.
- 692 Miles, J. W.: On the stability of heterogeneous shear flows, *Journal of Fluid Mechanics*, 10(4):496-508,
693 <https://doi.org/10.1017/S0022112061000305>, 1961.



- 694 Montégut, C. D. B., Madec, G., Fischer, A. S., Lazar, A., and Iudicone, D.: Mixed layer depth over the global ocean: An
695 examination of profile data and a profile-based climatology, *J. Geophys. Res.*, 109, C12003,
696 <https://doi.org/10.1029/2006JC004051>, 2004.
- 697 Muacho, S., da Silva, J. C. B., Brotas, V., Oliveira, P. B., and Magalhaes, J. M.: Chlorophyll enhancement in the central region
698 of the Bay of Biscay as a result of internal tidal wave interaction, *Journal of Marine Systems*, 136, 22–30,
699 <https://doi.org/10.1016/j.jmarsys.2014.03.016>, 2014.
- 700 Munk, W., and Wunsch, C.: Abyssal recipes II: Energetics of tidal and wind mixing. *Deep Sea Research, Part I: Oceanographic*
701 *Research Papers*, 45, 1977–2010, [https://doi.org/10.1016/S0967-0637\(98\)00070-3](https://doi.org/10.1016/S0967-0637(98)00070-3), 1998.
- 702 Nasmyth, P. W.: Oceanic turbulence, Ph.D. thesis, University of British Columbia, 71 pp, <https://doi.org/10.14288/1.0084817>,
703 1970.
- 704 Neto, A. V. N., and da Silva, A. C.: Seawater temperature changes associated with the North Brazil current dynamics, *Ocean*
705 *Dynamics*, 64, 13–27, <https://doi.org/10.1007/s10236-013-0667-4>, 2014.
- 706 New, A. L., and Pingree, R. D.: Local Generation Of Internal Soliton Packets In The Central Bay Of Biscay, *Deep-Sea*
707 *Research Part A-Oceanographic Research Papers*, 39 (9A), 1521 - 1534, [https://doi.org/10.1016/0198-0149\(92\)90045-U](https://doi.org/10.1016/0198-0149(92)90045-U),
708 1992.
- 709 New, A., and da Silva, J.: Remote-sensing evidence for the local generation of internal soliton packets in the central Bay of
710 Biscay, *Deep Sea Research Part I: Oceanographic Research Papers*, 49, 915–934, [https://doi.org/10.1016/S0967-](https://doi.org/10.1016/S0967-0637(01)00082-6)
711 [0637\(01\)00082-6](https://doi.org/10.1016/S0967-0637(01)00082-6), 2002.
- 712 Nugroho, D., Koch-Larrouy, A., Gaspar, P., Lyard, F., Reffray, G., and Tranchant, B.: Modelling explicit tides in the
713 Indonesian seas: An important process for surface sea water properties, *Mar. Pollut. Bull.*, 131, 7–18,
714 <https://doi.org/10.1016/j.marpolbul.2017.06.033>, 2018.
- 715 Osborn, T. R.: Estimates of the local rate of vertical diffusion from dissipation measurements, *J. Phys. Oceanogr*, 10, 83–89,
716 [https://doi.org/10.1175/1520-0485\(1980\)010<0083:EOTLRO>2.0.CO;2](https://doi.org/10.1175/1520-0485(1980)010<0083:EOTLRO>2.0.CO;2), 1980.
- 717 Prestes, Y. O., Silva, A. C., and Jeandel, C.: Amazon water lenses and the influence of the North Brazil Current on the
718 continental shelf, *Continental Shelf Research*, 160, 36-48, <https://doi.org/10.1016/j.csr.2018.04.002>, 2018.
- 719 Rainville, L., and Pinkel, R.: Propagation of Low-Mode Internal Waves through the Ocean, *Journal of Physical Oceanography*,
720 36:1220, 2006, <https://doi.org/10.1175/JPO2889.1>, 2006.



- 721 Ray, R. D., and Susanto, R. D.: Tidal mixing signatures in the Indonesian seas from high resolution sea surface temperature
722 data. *Geophys. Res. Lett.*, 43, 8115–8123, <https://doi.org/10.1002/2016GL069485>, 2016.
- 723 Rippeth, T. P., Palmer, M. R., Simpson, J. H., Fisher, N. R., and Sharples, J.: Thermocline mixing in summer stratified
724 continental shelf sea, *Geophys. Res. Lett.*, 32 (5), L05602, <https://doi.org/10.1029/2004GL022104>, 2005.
- 725 Ruault, V., Jouanno, J., Durand, F., Chanut, J., and Benshila, R.: Role of the Tide on the Structure of the Amazon Plume: A
726 Numerical Modeling Approach, *J. Geophys. Res.-Oceans*, 125, e2019JC015495, <https://doi.org/10.1029/2019JC015495>,
727 2020.
- 728 Sharples, J., and Zeldis, J. R.: Variability of internal tide energy, mixing and nitrate fluxes in response to changes in
729 stratification on the northeast New Zealand continental shelf. *New Zeal. J. Mar. Fresh.*, 55: 94 - 111,
730 <https://doi.org/10.1080/00288330.2019.1705357>, 2019.
- 731 Sheen, K.L., Brearley, J. A., Naveira Garabato, A.C., Waterman, S., Smeed, D. A. , Ledwell, J.R., Meredith, M.P. , St. Laurent,
732 L., Thurnherr, A.M., Toole, J.M., Watson, A. J.: Rates and mechanisms of turbulent dissipation and mixing in the Southern
733 Ocean: Results from the Diapycnal and Isopycnal Mixing Experiment in the Southern Ocean (DIMES), *J. Geophys. Res.*
734 *Oceans*, 118, 2774–2792, <https://doi.org/10.1002/jgrc.20217>, 2013.
- 735 Simpson, J. H., and Sharples, J.: Introduction to the physical and biological oceanography of shelf seas, Cambridge University
736 Press, pp. 1-24, <https://doi.org/10.1038/250404a0>, 2012.
- 737 Sprintall, J., Gordon, A. L., Koch-Larrouy, A., Lee, T., Potemra, J. T., Pujiana, K., and Wijffels, S.: The Indonesian Seas and
738 their impact on the Coupled Ocean Climate System, *Nat. Geosci.*, 7, 487–492, <https://doi.org/10.1038/NGEO2188>, 2014.
- 739 Stansfield, K., Garrett, C., Dewey, R.: The probability distribution of the Thorpe displacement within overturns in Juan de
740 Fuca Strait, *J. Phys. Oceanogr.*, 31, 3421–3434, [https://doi.org/10.1175/1520-0485\(2001\)031<3421:TPDOTT>2.0.CO;2](https://doi.org/10.1175/1520-0485(2001)031<3421:TPDOTT>2.0.CO;2),
741 2001.
- 742 St. Laurent, L. C., Garabato, A.N., Ledwell, J.R., Thurnherr, A.M., Toole, J.M., and Watson, A. J.: Turbulence and diapycnal
743 mixing in Drake Passage, *Journal of Physical Oceanography*, 42, 2143–2152, <https://doi.org/10.1175/JPO-D-12-027.1>,
744 2012.
- 745 Sutherland, G., Reverdin, G., Marié, L., and Ward, B.: Mixed and mixing layer depths in the ocean surface boundary layer
746 under conditions of diurnal stratification, *Geophys. Res. Lett.*, 41, 8469–8476, <https://doi.org/10.1002/2014GL061939>,
747 2014.



- 748 Takahashi, A., and Hibiya, T.: Assessment of finescale parameterizations of deep ocean mixing in the presence of geostrophic
749 current shear: Results of microstructure measurements in the Antarctic Circumpolar Current region, *Journal of Geophysical*
750 *Research: Oceans*, 124, 135–153, <https://doi.org/10.1029/2018JC014030>, 2019.
- 751 Tchilibou, M., Koch-Larrouy, A., Barbot, S., Lyard, F., Morel, Y., Jouanno, J., and Morrow, R.: Internal tides off the Amazon
752 shelf during two contrasted seasons: Interactions with background circulation and SSH imprints, *Ocean Science*
753 *Discussions*, 14, 1283–1301, <https://doi.org/10.5194/os-18-1591-2022>, 2022.
- 754 Thorpe, S. A.: Models of energy loss from internal waves breaking in the ocean, *Journal of Fluid Mechanics*, 836, 72–116,
755 <https://doi.org/10.1017/jfm.2017.780>, 2018.
- 756 Varona, H. L., Veeda, D., Silva, M., Cintra, M., and Araujo, M.: Amazon River plume influence on Western Tropical Atlantic
757 dynamic variability, *Dynamics of Atmospheres and Oceans*, 85, pp.1-15, <https://doi.org/10.1016/j.dynatmoce.2018.10.002>,
758 2018.
- 759 Wang, Y.-H., Dai, C.-F., and Chen, Y.-Y.: Physical and ecological processes of internal waves on an isolated reef ecosystem
760 in the South China Sea, *Geophysical Research Letters*, 34(18), <https://doi.org/10.1029/2007gl030658>, 2007.
- 761 Whalen, C. B., Talley, L. D., and MacKinnon, J. A.: Spatial and temporal variability of global ocean mixing inferred from
762 Argo profiles, *Geophys. Res. Lett.*, 39:L18612, <https://doi.org/10.1029/2012GL053196>, 2012.
- 763 Xie, X. H., Cuypers, Y., Bouruet-Aubertot, P., Ferron, B., Pichon, A., Lourenço, A., and Cortes, N.: Large-amplitude internal
764 tides, solitary waves, and turbulence in the central Bay of Biscay, *Geophysical Research Letters*, 40(11), 2748–2754,
765 <https://doi.org/10.1002/grl.50533>, 2013.
- 766 Xu, P., Yang, W., Zhu, B., Wei, H., Zhao, L., and Nie, H.: Turbulent mixing and vertical nitrate flux induced by the semidiurnal
767 internal tides in the southern Yellow Sea, *Continental Shelf Research*, 208, 104240,
768 <https://doi.org/10.1016/j.csr.2020.104240>, 2020.
- 769 Yang, W., Wei, H., Zhao, L., and Zhang, J.: Turbulence and vertical nitrate flux adjacent to the Changjiang Estuary during
770 fall, *Journal of Marine Systems*, 212: 103427, <https://doi.org/10.1016/j.jmarsys.2020.103427>, 2020.
- 771 Zaron, E. D., Capuano, T. A., and Koch-Larrouy, A.: Fortnightly variability of Chl a in the Indonesian seas, *Ocean Sci.*, 19,
772 43–55, <https://doi.org/10.5194/os-19-43-2023>, 2023.
- 773 Zhao, Z., Alford, M. H., Girton, J. B., Rainville, L., and Simmons, H. L.: Global Observations of Open-Ocean Mode-1 M2
774 Internal Tides, *J. Phys. Oceanogr.*, 46, 1657–1684, <https://doi.org/10.1175/JPO-D-15-0105.1>, 2016.

<https://doi.org/10.5194/egusphere-2024-2548>

Preprint. Discussion started: 30 August 2024

© Author(s) 2024. CC BY 4.0 License.



775 Zhao, Z., Alford, M. H., and Girtton, J.B.: Mapping low-mode internal tides from multisatellite altimetry, *Oceanography*,
776 25(2):42–51, <https://doi.org/10.5670/oceanog.2012.40>, 2012.